5-2021

# Next Generation Energy Storage: An Examination of Lignin-based Carbon Composite Anodes for Sodium Ion Batteries through Modeling and Simulation

Dayton G. Kizzire
*University of Tennessee, Knoxville*, dkizzire@vols.utk.edu

To the Graduate Council:

I am submitting herewith a dissertation written by Dayton G. Kizzire entitled "Next Generation Energy Storage: An Examination of Lignin-based Carbon Composite Anodes for Sodium Ion Batteries through Modeling and Simulation." I have examined the final electronic copy of this dissertation for form and content and recommend that it be accepted in partial fulfillment of the requirements for the degree of Doctor of Philosophy, with a major in Materials Science and Engineering.

David J Keffer, Major Professor

We have read this dissertation and recommend its acceptance:

David J. Keffer, David P. Harper, Orlando Rios, Haixuan Xu

Accepted for the Council:

Dixie L. Thompson

Vice Provost and Dean of the Graduate School

(Original signatures are on file with official student records.)

# Next Generation Energy Storage: An Examination of Lignin-based Carbon Composite Anodes for Sodium Ion Batteries through Modeling and Simulation

**A Dissertation Presented for the**
**Doctor of Philosophy**
**Degree**
**The University of Tennessee, Knoxville**

**Dayton G. Kizzire**
**May 2021**

# DEDICATION

I dedicate this dissertation to my amazing, fun, and loving wife, Farren. Farren, thank you for the great amount of laughter, love, support, patience, and understanding as I have worked to obtain this Ph.D. I could not have gotten here without you.

To my parents, Lori and Billy, for loving me every step of the way and fostering my love for learning and discovery. Thank you for your unending support, your uplifting words of encouragement, and for your constant prayers.

To my brother Cole, for your love and jokes and all the laughter they bring me.

To my in-laws, Rod and Marjorie. Thank you for all the love and support you have given to me and Farren. Thank you for your wise words and your prayers.

# ACKNOWLEDGEMENTS

My sincerest thanks and eternal gratitude go to my advisors, Dr. David Keffer and Dr. David Harper. Their guidance, encouragement, and mentorship has had an incredible impact on my professional and personal self. Dr. Keffer, thank you for teaching me to code and facilitating my growth as a researcher and as a person. Dr. Harper, thank you for teaching me experimental techniques and for the wonderful experience of CABLE. I also thank Dr. Xianfeng Ma, your insights into high performance computing have been very valuable and your assistance made portions of this work possible. I would like to extend my thanks to my committee members, Dr. Orlando Rios and Dr. Haixuan Xu for your valuable advice and all that I learned from you.

I would like to thank members of my research group Valerie García-Negrón and Lu Yu for their experimental support and all of the laughter, tea, and time we have shared. I would also like to extend sincere thanks to Alexander Richter, your assistance was incredibly valuable and I am greatly appreciative.

I am grateful for all of the professors and staff in the Materials Science and Engineering Department for their instruction and support.

My special thanks go out to the United States Department of Agriculture which supported this work and to the ISAAC and XSEDE supercomputing centers for making this work possible through your facilities.

# ABSTRACT

The current energy market relies heavily on fossil fuel sources; however, we are amidst a momentous shift towards wind, solar, and water based renewable energies. Large-scale energy storage allows renewable energy to be stored and supply the grid with consistent energy despite changing weather conditions. Improvements to large-scale energy storage in terms of cost, safety, and sustainability are crucial to wide-scale adoption. A promising candidate for large-scale energy storage are sodium-ion batteries using hard carbon anodes. Sodium is globally available, cheaper, and more sustainable than lithium, but requires a different anode structure. A sustainable hard carbon anode with excellent Li-ion performance has been manufactured from lignin, a byproduct of the paper and bio-ethanol industries. The carbon composite generated from lignin is composed of nanoscale crystallites dispersed in an amorphous graphene matrix whose structure is highly dependent on manufacturing process; however, the sodium-ion storage mechanisms for these lignin-based hard carbons are not well known.

The purpose of the following work is to elucidate the Na-ion storage mechanisms for these lignin-based hard carbons and develop process-structure-property-performance (PSPP) relationships for them so an optimal Na-ion anode can be manufactured. To this end, reactive molecular dynamics simulations of lignin-based carbon composites were conducted with both lithium and sodium to compare the binding energies and mechanisms as well as their respective diffusive properties. It was found that lithium-ions prefer to localize in the hydrogen dense interfacial regions of the carbon composites while sodium prefer to adsorb to the surfaces of graphene fragments as well as the outer faces and edge-intercalation positions of the crystallites. At higher porosity, sodium shows a tendency to aggregate in the porous regions along curved planes of graphene, which gives the Na-ions the highest diffusion rate of all systems studied.

To aid in determining the PSPP relationships of LBCCs, synchrotron x-ray scattering was performed, and models were created and refined using the Hierarchical Decomposition of the Radial Distribution Function (HDRDF) technique and software (now highly generalized). PSPP relationships with respect to processing temperature were quantitatively and qualitatively determined for the lignin-based carbon composites.

# TABLE OF CONTENTS

# LIST OF TABLES

# LIST OF FIGURES

# INTRODUCTION

Rechargeable Li-ion batteries have been one of the most crucial technologies of the past 30 years, allowing advances in modern portable electronics, electric vehicles, as well as storage of energy from intermittent renewable energy sources such as solar and wind. In our current world, where efficiency, sustainability, and cleaner energy are priorities, high-performance batteries manufactured with bio-based and renewable materials are a necessity. Modern li-ion batteries consist of three essential parts, a graphitic anode, a lithium and metal oxide cathode, and a porous separator immersed in a non-aqueous liquid electrolyte [1]. While charging, Li-ions migrate from the cathode, through the separator, to the anode and intercalate between planes of graphite to form lithiated graphite. When discharging, electrons are released to the external circuit as the Li-ions migrate back to the cathode host structure. Graphitic carbon has been the backbone of anode materials for nearly 30 years and has had little innovation in this time when compared to cathode materials that have been meticulously researched and improved [2-8]. Through this work, we aim to improve the modern graphitic anode and explore utilizing sodium rather than lithium as the charge carrying ion.

## *1.1 Modern Graphitic Anodes*

It is important to note that graphite is not readily available domestically in the United States and is mostly imported from countries with large graphite mining operations or large petroleum processing plants from which petroleum coke can be refined into graphite. Over 70% of the worlds graphite supply comes from China due to the natural abundance [9]. Modern graphitic anodes for li-ion batteries rely on reversible intercalation of li-ions from spherical graphite particles (SPGs). SPGs are manufactured from natural flake (60% loss) and synthetic (coke) graphite through milling and have a resulting diameter of 5 to 20 microns [10]. Most SPGs are then coated in a nanolayer of non-graphitic carbon. The resulting morphology has shown to increase resistance to degradation from electrolyte interactions and improves high-rate capacity, reversible capacity, coulombic efficiency, and irreversible capacity over flake graphite [10-12]. Aspects of improving current graphitic anodes include increasing charge capacity, long term cyclability, safety as well as reducing mining and petroleum product pollution by finding a renewable, sustainable, and domestic source of graphite.

## *1.2 Lignin Based Carbon Composites as Anode Material*

Previous studies by Tenhaeff, Rios, More, and McGuire suggested a solution for a more environmentally friendly and sustainable source of high performance graphitic anodes

through lignin [13]. Lignin is the second most abundant natural organic material on earth and over 100 million tonnes of lignin is generated each year through the commercial paper and bio-ethanol industries [14]. Lignin is an organic polymer found in the cell walls of woody plants and affects the stability, stiffness and flexibility of plants [15]. It has an aromatic, cross-linked, heterogenous, amorphous structure composed of varying amounts of p-hydroxyphenyl (H), guaiacyl (G), and syringyl (S) phenolic units depending on the plant species. Commercially generated lignin was historically burned for heat and power in the aforementioned industries. With modern advances in lignin processing, lignin can now be considered a low-cost, renewable bio-feedstock for the manufacturing of graphite, thermoplastics, carbon fibers, phenolic resins, and lignin-based polymers among many other products currently sourced from petroleum [13,14,16,17].

Work by García-Negrón *et al.* shows isolation of high-purity lignin along with subsequent pyrolysis and reduction at 1050°C yields a composite composed of graphitic nanoscale crystallite spheroids dispersed in an amorphous carbon matrix and have shown success in use as high-performance anodes in Li-ion batteries [18]. Higher reducing temperatures produce larger crystallites with increasing crystalline volume fraction. These lignin-based carbon composites have crystallites sizes of 1 to 40 nm, 1000 times smaller than that of SPGs used in modern li-ion batteries. The unique morphology and nanoscale structure present in anodes fabricated from lignin pyrolyzed and reduced at 1050°C have been shown to have specific capacities of up to 444 mAh $g^{-1}$ with coulombic efficiency of 98% sustained for extended galvanostatic cycles in coin cell batteries [18]. This 20% increase in specific capacity over the theoretical limit of 372 $mAhg^{-1}$ for graphite was explained by the modelling works of McNutt *et al.* where it was shown that these lignin-based carbon-composites have a fundamentally different storage mechanism for li-ions compared to standard graphitic anodes [19]. Specifically, when the graphitic crystallites are sufficiently small, li-ions prefer to localize in the interfacial regions between the graphitic nanocrystallites and amorphous fragments of graphene that constitute the amorphous carbon matrix [20]. The resultant idea from the combined works of Tenhaeff, McNutt, and García-Negrón *et al.* is that lignin can be used to create high performance graphitic anodes where the features that control localization and energetics of li-ions in the carbon-composite anode such as crystallite size, crystalline volume fraction, and composite density can be optimized through choice of lignin feedstock, processing conditions, and reduction temperature [18-21].

### *1.3 Understanding the Carbon-Composite Structure*

Understanding the relationship between the atomic and meso-scale structure and choice of feedstock and processing conditions of the lignin-based carbon-composite anode is critical

to optimizing the exceptional properties shown in the previous works. In materials characterization, there is often no one-size-fits-all approach and the technique used is largely dictated by the physiochemical structure of the material in question. However, as explained in the book by Takeshi Egami and Simon Billinge, *Underneath the Bragg Peaks: Structural Analysis of Complex Materials*, the local atomic environment is often characterized via the radial distribution function (RDF) or *g(r)* where *r* is the separation between atoms. Neutron and x-ray scattering experiments yield the total scattering intensity function *S(Q)* which includes both Bragg and diffuse scattering and can be Fourier transformed to real space to represent the RDF. The RDF is an effective function for evaluating the local structure of powder, single crystal, or liquid materials containing amorphous or crystalline domains and isotropic or anisotropic orientations [22,23]. In battery specific research it can also help define local order changes from cycling, nano-phase quantifications, and ion storage mechanisms [19,21,24-29].

When studying complex materials, interpretation of the RDF can present a significant challenge due to the nature of scattering from multiple nanoscale phases and/or amorphous phases. The extent of this problem can be lessened through the use of high energy neutron sources and synchrotron x-ray sources where the small wavelength, high brilliance, low beam divergence, and 2-d scattering detectors can be used to characterize nanoscale features that would not be distinguishable using standard lab x-ray sources [22]. Since the lignin-based carbon composite anode has significant amorphous domains, both high energy neutron scattering and synchrotron x-ray diffraction are used to help determine structure.
The process of ascribing structural features of nanomaterials to specific peaks and features of an experimentally obtained RDF can be arduous and confusing. By generating a model of the nanomaterial in question and simulating its RDF, researchers can directly attribute structural characteristics to features present in the calculated RDF [22,29,30]. Traditionally, complex nanostructured materials are modelled with large scale molecular dynamics (MD) simulations to form a hypothetical structure and generate a corresponding RDF to be compared to experiment [27]. This is not normally an iterative process as the initial creation and subsequent alterations to the structure and constituent particle size of complex nanomaterials in MD simulations is a laborious and computationally expensive process [31].

The task of developing a generalized software tool for the extraction of structural information from the RDF of complex nanomaterials is ongoing with significant strides being made by the developers of RMCprofile [32-34] and DISCUS [35,36]. A new and significantly efficient approach for the interpretation of RDFs of complex materials is the Hierarchical Decomposition of the RDF (HDRDF) proposed by Oyedele *et al.* where

theory and tractable models at both atomic and mesoscales are combined to generate the RDF free from curve fitting techniques [31]. Version 2 of HDRDF was developed in MATLAB by García-Negrón *et al.* and tested against MD simulations of the pyrolyzed lignin carbon composite [37]. HDRDF version 2 was shown to correctly capture the contributions of the crystalline and amorphous phases and their interface in the modelled RDF, while achieving a reduction in computational cost by six orders of magnitude compared to MD simulation [37]. HDRDF v2 also allowed iterative refinement of the model, but only with spherical nanoparticles. Chapter 3 of this work showcases the third version of HDRDF (henceforth called HDRDF) developed in C++ and expanded to be user-friendly and to allow arbitrary particle geometry. Figure i.1 below shows the decomposition of the RDF with the corresponding features present in the composite.

### *1.3 Understanding Ion Localization in Carbon-Carbon Composites with ReaxFF*

Knowledge of ion localization in carbon-carbon composite anode material is a key element of understanding the large specific capacities shown in testing. Normally, density functional theory (DFT) is employed to accurately describe chemical reactions and preferential localization between ions and host materials [38-42]; however, to capture the mesoscale order of the carbon-carbon composite and its effect on ion localization it is necessary to have large simulation sizes with thousands of atoms [19]. Since DFT is excessively computationally expensive for large system sizes and for the timescale needed to simulate ion movement through the carbon composite, we employ reactive molecular dynamics simulations using ReaxFF to simulate the charged carbon composites [43]. ReaxFF are empirical force field potentials trained with structure and energy data from DFT calculations to allow modelling of electron redistribution through reaction, charge transfer, and ion movement on reasonable timescales with substantially less computational resources [43].

As mentioned above in section 1.2, the work of McNutt *et al.* has shown that lithium are preferentially localized in the hydrogen dense interfacial region of the carbon-composite anode instead of intercalated between planes of graphitic crystallites as occurs in modern SPG anodes [19]. According to previous research by Papanek *et al.* the H/C ratio plays a direct role in determining ion storage capacity [44]. The combination of these two ideas with the knowledge that new nanocomposite electrodes are improving electrochemical performance in sodium-ion batteries lead us to believe that the lignin-based carbon-composite anode could be a viable host structure for sodium [45]. The sodium ion battery is at the forefront of battery research currently due to the worldwide and vast availability of sodium and its radical price difference compared to lithium [29,46-48]. Chapters 1 and 2 of this work focus on the energetics and preferential localization of sodium in the carbon-composite anode.

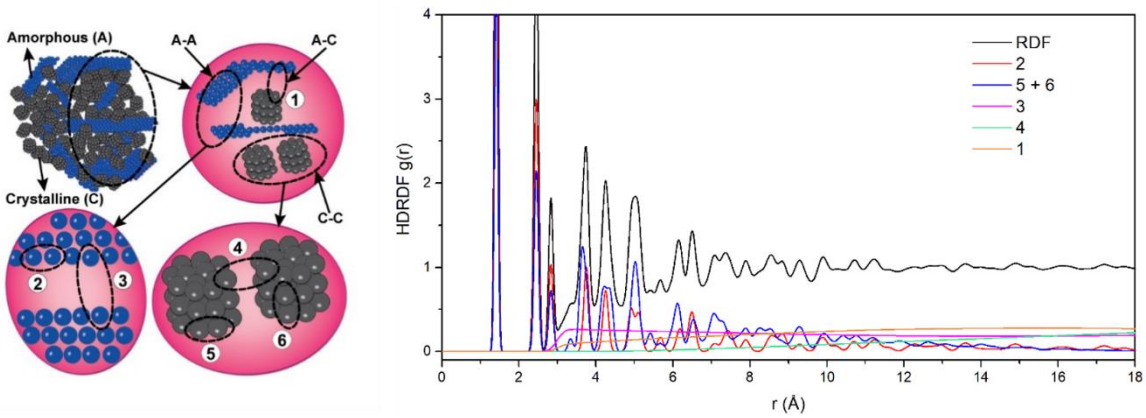


**Figure i.1:** Schematic of the hierarchical decomposition of a composite and corresponding contributions to the RDF. Numbers represent pairs as follows: [1)] amorphous-crystallite, [2)] A-A intraplanar, [3)] A-A interplanar, [4)] C-C intercrystallite, [5)] C-C intracrystallite intraplanar, [6)] C-C intracrystallite interplanar.

# CHAPTER I

# Lithium and Sodium Ion Binding in Nanostructured Carbon Composites

A version of this chapter was originally published by by Dayton G. Kizzire, Alexander M. Richter, David P. Harper, and David J. Keffer

Kizzire, D. G., Richter, A. M., Harper, D. P. & Keffer, D. J. Lithium and sodium ion binding in nanostructured carbon composites. Molecular Simulation, 1-10, doi:10.1080/08927022.2020.1800689 (2020).

The following article's content is unchanged from the above publication except for format and some spelling changes (British English to American English). The publication is two-column format and below the article is in single-column format. The numbers in the section headings have also been removed. Figure and Table positions have been moved slightly to accommodate the required format.

Credit authorship contribution statement:
Dayton G. Kizzire: Investigation, computational resource acquisition, simulations, formal analysis, writing (original draft), data visualization, data curation. Alexander M. Richter: simulations, data visualization, computational resource acquisition. David P. Harper: Writing – review & editing. David J. Keffer: Conceptualization, methodology, computational resource acquisition, supervision, formal analysis, investigation, Writing – review & editing.

## Abstract

High charge capacity in lithium and sodium ion batteries can be achieved using anodes composed of nanostructured carbon composites. The tailoring of the nanostructure to achieve both high loading and low irreversible binding depends upon the binding mechanisms of the ion. In this work, reactive molecular dynamics simulations are performed on model carbon composite anodes to investigate and to compare the binding mechanisms of lithium and sodium ions. In composites composed of both crystalline and amorphous domains, lithium ions bind preferentially at the interface between the amorphous and crystalline domains, rather than via the standard intercalation mechanism observed in graphitic anodes. In these same composites, sodium ions bind preferentially in the crystalline domain, even though intercalation of sodium in graphitic anodes is not a viable mechanism for charge storage. The difference in mechanisms is explained through a comparison of the binding energies in the carbon composite to the energies of the respective metals and metal hydrides.

## Introduction

High-energy-density batteries are a necessity to meet the ever-growing energy and power demands from electric vehicles, phones, medical equipment, military devices and large-scale energy storage. Researchers from around the globe have expended great effort through experiments and simulations to increase the charge capacity, cycle life, energy density and safety of lithium-ion batteries (LIBs). The simulation of LIB graphitic anodes normally includes nanosystems consisting of multiple phases and important interfacial regions where reactions and diffusion are coupled. Chemical reactions can be accurately described with density functional theory (DFT) calculations, but when combined with large system sizes required to characterised a disordered environment and the timescale needed to simulate ion movement through anode material, DFT quickly becomes excessively computational expensive [49,50]. To remedy this problem, empirical force field potentials are trained with structure and energy data from DFT calculations to allow modelling of electron redistribution through reaction and charge transfer on reasonable timescales with substantially less computational resources [43]. These reactive interaction potentials, such as the reactive force field (ReaxFF) potentials, have no discontinuity in energy or forces, which allows modelling the formation and dissociation of chemical bonds. ReaxFF also includes both van der Waals forces and coulombic interactions that play vital roles in the simulation of graphitic anodes [51,52].

While lithium-ion batteries have been the standard for high-performance batteries for the past thirty years, new demand for energy storage in electric vehicles and largescale grid applications has presented a large problem for LIBs as lithium is not a naturally abundant element and lithium-containing precursors are unevenly distributed globally [53]. These problems make lithium an unfavourable choice for large-scale energy storage applications. Alternatively, sodium-ion batteries (SIBs) have come to the forefront as an option for large-scale energy storage because, unlike lithium, sodium is abundant, cheap and distributed globally. However, sodium is non-functional in traditional graphitic anodes with the most likely reason being the lower energetic stability of Na-GICs compared to sodium metal [54,55]. Hard carbons, derived from biomass and highly porous, offer a solution to this problem through the storage of ions in porous and interfacial regions rather than intercalated between planes [56,57].

Previous studies have suggested carbonised lignin as a solution for low-cost, high-performance anode material [13,18,58]. Lignin is a class of aromatic polymers with an amorphous nd cross-linked three-dimensional structure with high carbon concentration. Lignin is found in woods and grasses and serves as a low-cost, renewable bio-feedstock for complex carbon composites. Processing and pyrolysis of lignin produce a graphitic composite composed of nanoscale carbon crystallite spheres dispersed in an amorphous carbon matrix [13,30,59]. The crystallite radius, crystalline volume fraction, density and

nanostructure are dependent upon pyrolysis temperature and lignin feedstock choice [13,21]. It has been previously shown that the nanocrystallite particle size is strongly correlated to both Li-ion intercalation capacity and chemical activity in carbon composites [60,61]. These graphitic nanocomposites have success in use as high-performance anodes in Li-ion batteries [18,58,60]. In previous studies where lignin sourced carbons are included in the anode of a Li-ion half-cell battery, the battery proved to have a superior charge capacity, high reversible capacity, low irreversible capacity loss and high cycle life when charged with lithium [18,62].

In previous computational studies, the energetics and nanoscale structure of both graphite and singular graphene planes have been extensively studied [63-66], and with the current interest in Li-ion alternatives to energy storage spiking and the development of carbon composite anode systems with comparable charge capacity, studies of carbon composites for use in energy storage have accelerated [67]. To aid in this discovery of new energy storage materials in this emerging field, Raju et al. [51] developed ReaxFF potentials to describe Li-ion intercalations in both perfect and defective carbon systems.

McNutt et al. [19,30] created several large-scale carbon composites that effectively modelled the lignin sourced carbon composites. A range of crystallite radii were studied to determine the effect of crystallite radius on ion distribution within the nanocrystallites. Reactive molecular dynamics (MD) simulations of these lithiated carbon composites and subsequent analysis through radial distribution functions (RDF) as well as energy and charge distributions led to defining a fundamentally new storage mechanism for Li-ions [19]. These simulations demonstrated the most favorable localization of Li-ions occurs in the interfacial regions between the nanocrystallites and the amorphous graphene fragments and allows Li-ions to be stored at a greater density than when intercalated into graphite [19]. Hydrogen is present in the interfacial region because it terminates the graphene sheets that compose both the nanocrystallites and the amorphous domain. The terminating hydrogen plays an important role in stabilizing lithium as shown by McNutt et al. [19].

Hjertenæs, Nguyen and Koch [68] developed ReaxFF potentials for sodium interactions in both graphitic and disordered carbons. It was found that there is a high affinity for Na-ions to bind to under-coordinated carbons along edge planes of graphitic crystallites and with a large enough chemical potential, Na-ions will easily penetrate pores and cavities in a graphic structure until saturated [68].

To better understand ion localization in complex carbon composites, we chose a small subsystem of McNutt's [30] large carbon composite consisting of a single spherical graphitic nanocrystallite embedded in an amorphous carbon matrix with hydrogen-terminated edges. To discover if the same binding mechanism observed in carbon nanocomposites containing Li-ions holds for Na-ions, the single carbon composite was simulated under a range of conditions. Lithium and sodium ions at high and low

concentrations are studied based on initial conditions either intercalated between planes of the nanocrystallite or, separately, inserted into the amorphous phase. We compare lithium and sodium-ion systems using both energetic and structural descriptors to differentiate between the binding locations and mechanisms for lithium and sodium. It is important to note that this work examines an idealized carbon composite system as a fraction of the anode without electrolyte interaction. It is currently unclear how oxidation from electrolyte decomposition would impact ion binding in these systems.

## Methods

The carbon composite modelled in this work was designed to emulate the experimentally produced carbon composite structure created from lignin by Tenhaeff et al. [13]. The construction of the carbon composite followed the procedure of McNutt [30]. The initial carbon nanocrystallite model was constructed by cutting a sphere with diameter14 Å from bulk AB stacked graphite, removing any singularly bonded carbons and terminating all edge carbons with hydrogen [19]. The nanocrystallite was then embedded into a matrix of amorphous carbon. The amorphous carbon was added as randomly oriented sheets of graphene, cut to avoid overlap with crystallites or other sheets in the amorphous domain, then hydrogen terminated. The system was then relaxed, which resulted in some shifting of the planes in the nanocrystallites and bending of the sheets in the amorphous domain. These plane distortions were quantified by McNutt et al. and are representative of the disordered nature of the lignin-based carbon composites being modelled [69].

To compare the binding mechanisms of lithium and sodium inserted into carbon composites, eight simulations were performed that represent a complete $2 \times 2 \times 2$ design matrix variating ion type (lithium or sodium), ion loading (high and low) and initial placement of ions (intercalated in the nanocrystallite or inserted in the amorphous domain). In the crystalline domain, the initial lithium positions correspond to favorable binding sites for lithium intercalated in bulk graphite. In the amorphous domain, the initial lithium positions were placed randomly to avoid overlap followed by minimization and equilibration. The ‘high’ ion loading corresponds to 22.7 mAh $g^{-1}$ and the ‘low’ ion loading corresponds to 1.62 mAh $g^{-1}$. Coin cells using lignin-based anodes have shown ion loading greater than the theoretical capacity of graphite (372 mAh $g^{-1}$) [18]. Here, the simulations are limited to significantly lower ion loadings in order to clearly distinguish between binding in the crystalline and amorphous domains.

The reactive MD simulations were carried out in LAMMPS [29]. The ReaxFF potentials of Raju et al. [4] and Hjertenæs et al. [27] were used for the lithium and sodium systems respectively. The simulation cells contained 1964 atoms (136 crystallite carbon, 1188 amorphous carbon, 626 hydrogen and 14 ions) for high loading systems and 1951

atoms for low loading systems (same composite but only 1 ion). Each data production simulation ran in a cubic simulation cell for 67 ps with a timestep of 0.25 fs in the canonical NVT ensemble at 298 K.

In order to evaluate the energetic favorability of the ions in the composite compared to other states, four additional simulations were performed for lithium metal, lithium hydride, sodium metal and sodium hydride. This second set of simulations used the same ReaxFF potentials and timestep. The pure metal and hydride simulations contained 128 and 2744 atoms, respectively. The optimal lattice parameter was determined via energy minimization. A subsequent simulation in the NVT ensemble at 298 K was performed to determine the energy. Finally, the empty carbon composite was simulated with both ReaxFF potentials to verify carbon and hydrogen were treated the same way.

The average energies and standard errors reported below were based on statistical analysis of individual ion energies over the course of the equilibrated simulation, separated into 10 blocks for block-averaging.

## Results and Discussion

### *Uncharged carbon composite*

In order to verify the description of carbon and hydrogen was consistent between potentials, the uncharged carbon composite was simulated with both the ReaxFF potentials of Raju et al. [51] and Hjertenæs et al. [68]. The two potentials yield identical simulation results, which is consistent with the description of the procedure for extending the potential to sodium, in which the carbon and hydrogen interaction was not modified [68]. In Figure 1.1, the energy distributions of carbon and hydrogen are reported. Although the system is composed of a crystalline domain surrounded by an amorphous matrix, the bimodal distribution of energy for carbon in Figure 1.1(a) does not correspond to these two phases. Individual distributions of the carbons in the graphitic nanocrystallite and in the graphene fragments of the amorphous domain both possess a similar bimodal distribution (not shown). Rather, the two modes reflect energy differences between carbons located in the interior of a graphene sheet (whether stacked as part of a nanocrystallite or not), in which the carbon atom is bonded to three other carbon atoms, and a carbon at the edge of a sheet, in which the carbon atom is bonded to two carbon atoms and one terminating hydrogen atom. The distribution of hydrogen energies in Figure 1.1(b) is broad and reflects the heterogeneity of the carbon composite.

### *Charged composites*

In the following section of work, we compare lithium and sodium in the four configurations, corresponding to a low and high loading in which the ions are initially placed in the crystalline and amorphous domains. Figure 1.2 shows a snapshot from each

of the simulations with the lithium ions. Figure 1.3 shows a snapshot from each of the simulations with the sodium ions.

In the simulations that contain lithium ions initially placed intercalated in the nanocrystallite, the atoms are observed to diffuse out from the crystallite and come to rest at the interface between the crystalline and amorphous domain. This behaviour can be observed at both high (Figure 1.2(a)) and low (Figure 1.2(c)) loadings. This movement of lithium ions to the interface has been previously reported [19,20]. The driving force for this redistribution is discussed in greater detail below. The simulations in which lithium ions are initially placed in the amorphous domain conclude with lithium remaining in the amorphous domain, although, in the high loading case, some ions migrate to the interface with the crystallite.

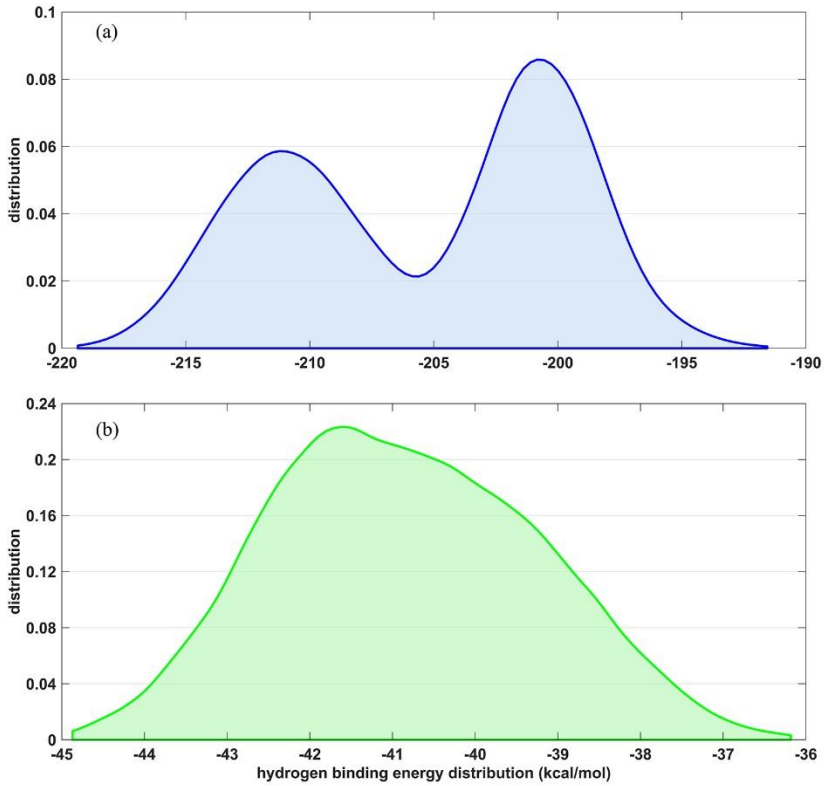


**Figure 1.1:** Distributions of individual atomic energies for (a) carbon and (b) hydrogen in the uncharged system.

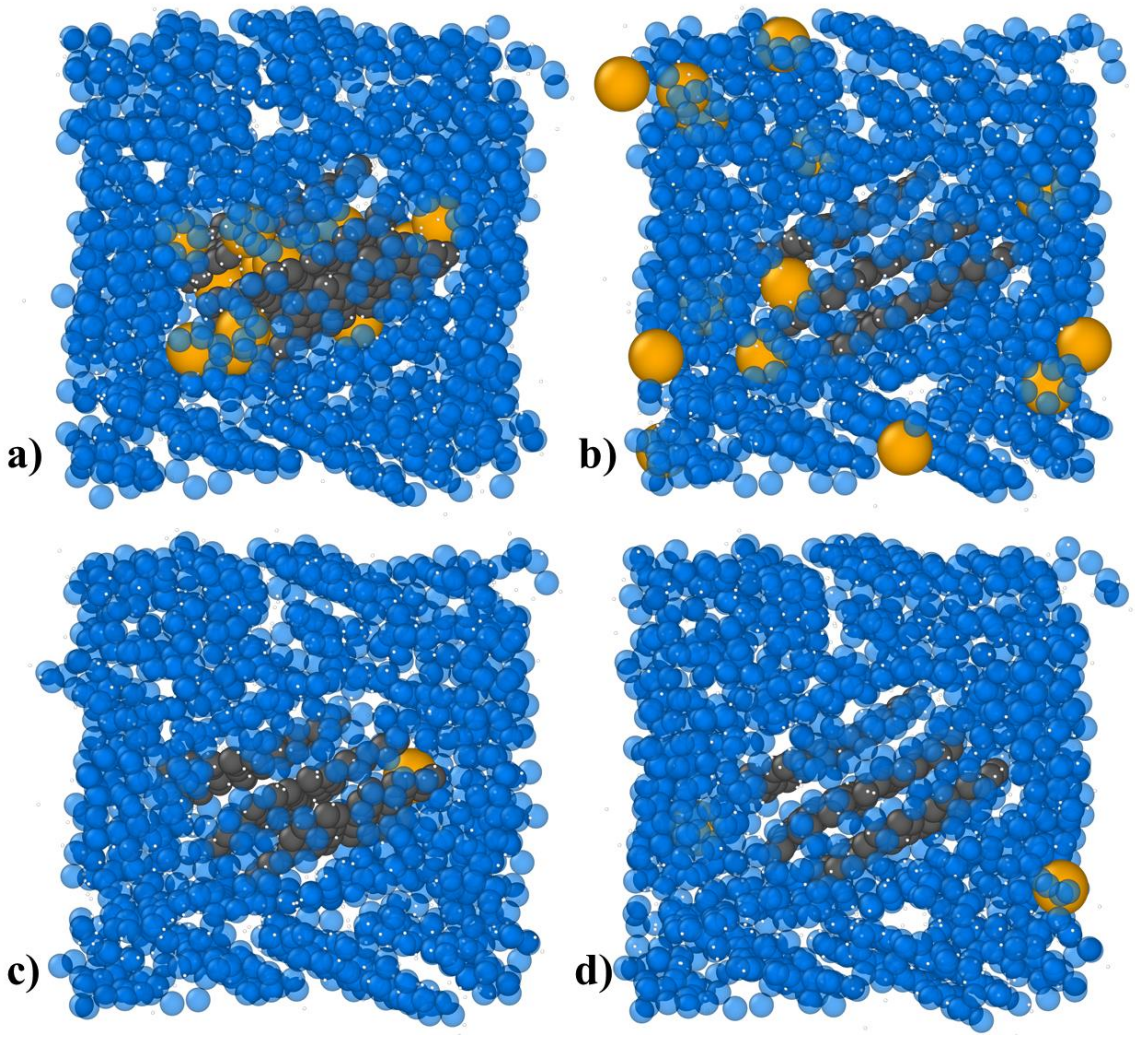


**Figure 1.2:** Snapshots of the carbon composite charged with lithium ions for (a) high loading in the crystalline domain, (b) high loading in the amorphous domain, (c) low loading in the crystalline domain and (d) low loading in the amorphous domain. Colour code: Carbon in the graphitic nanocrystallites is gray. Carbon in the amorphous domain is transparent blue. Hydrogen are small white points. Lithium ions are yellow.

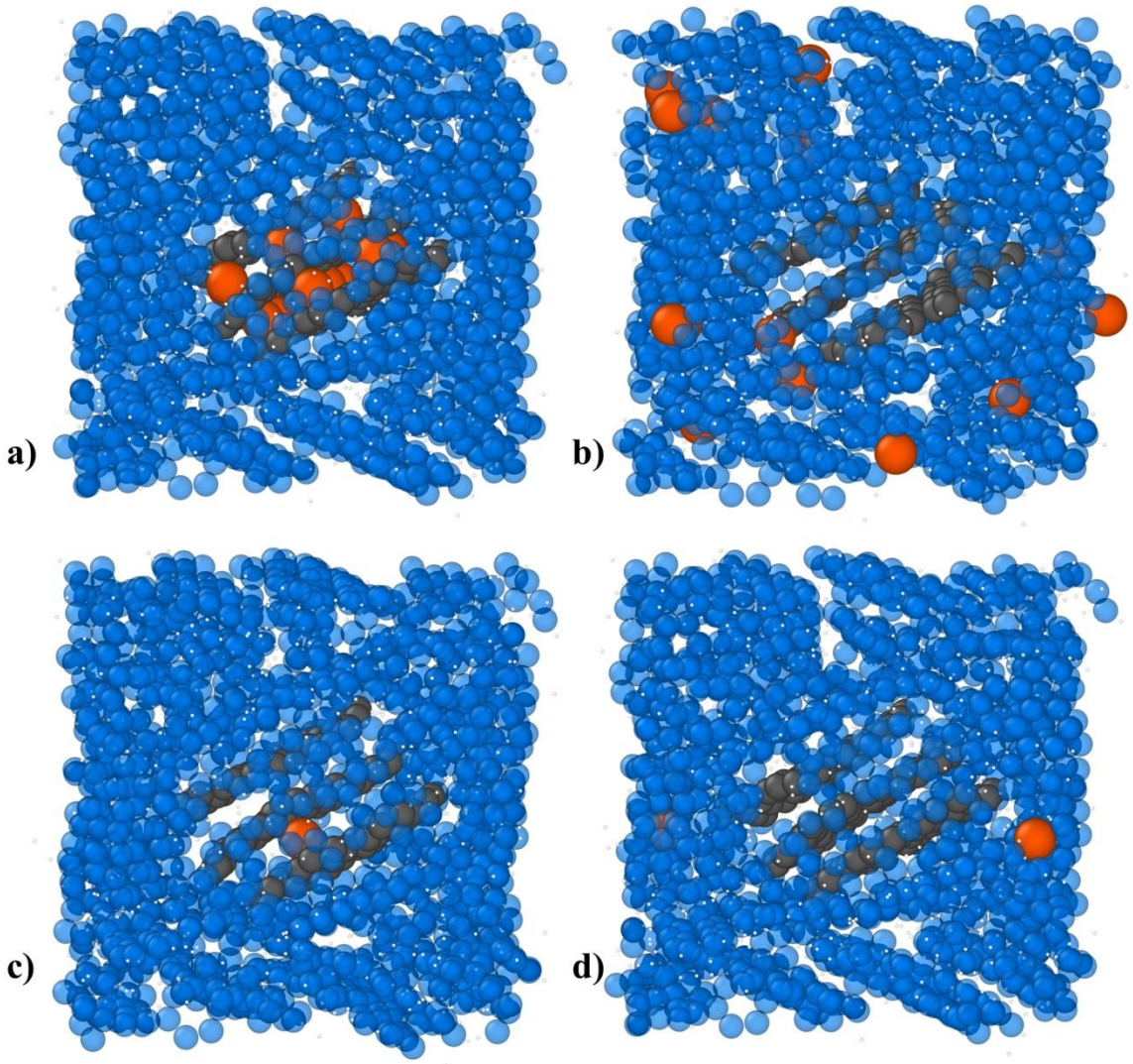


**Figure 1.3:** Snapshots of the carbon composite charged with sodium ions for (a) high loading in the crystalline domain, (b) high loading in the amorphous domain, (c) low loading in the crystalline domain and (d) low loading in the amorphous domain. Colour code:Carbon in the graphitic nanocrystallites is gray. Carbon in the amorphous domain is transparent blue. Hydrogen are small white points. Sodium ions are orange.

The distribution of ion binding energies for the four lithium-containing composites is shown in Figure 1.4(a). It is immediately apparent that there exists a broad distribution of binding energies, again reflecting the heterogeneity at the atomic scale of the carbon composite. If the binding mechanism were due to physisorption, one would expect that the low loading systems would display more favorable binding energies as the first ions in would occupy the most favorable binding sites and subsequent ions would be forced to occupy less energetically favorable sites. However, lithium ions in these systems do not obey this behavior. It is clear in the distributions in Figure 1.4(a) that the high loading systems push the distribution into stronger binding. The average values reported in Figure 1.5(a) confirm this observation. For both crystalline and amorphous initial positions, the high loading cases have more favorable binding energies compared to the low loading cases. Furthermore, for both the high and low loading case, the simulations that began with the ions in the amorphous phase are more strongly bound compared to those at the same loading with ions initially in the crystalline phase. McNutt et al. observed this behavior and attributed it to two factors: aggregation of lithium correlates with stronger binding energies and association of lithium with terminating hydrogen [30]. Because lithium is better able to aggregate at high loadings, the first factor explains why the binding energy becomes more favorable as the loading increases. Since there is no hydrogen in the interior of the nanocrystallite, the second factor explains why lithium migrates from the intercalated initial positions and moves into the interface between the amorphous and crystalline domains. Therefore, lithium capacity is strongly dependent on this interfacial area. It has been shown that composite anodes with small nanocrystallites are capable of lithium storage capacity in excess of the theoretical limits of 372 mAh/g of bulk graphite [18].

It is worth mentioning briefly that these relatively short MD simulations cannot capture the complete relaxation of the system. If the simulation were allowed to proceed for an infinitely long period of time, the same average thermodynamic properties should be obtained regardless of whether ions were initially placed in the crystalline or amorphous domains. However, two advantages of small systems are (i) that the simulations can be run sufficiently long to observe some diffusive processes and (ii) the impact of single atoms can be clearly followed. For example, in Figure 1.6, the exit of a single lithium atom from the crystallite can be observed. A corresponding change in the potential energy with the ion departure captures the relationship between the phase of the ion and its energetic state.

The simulations in which the carbon composites are charged with sodium display a different behavior than the lithium charged systems. As can be observed in the snapshots of Figure 1.3(a,c), sodium ions that are initially placed in the carbon composite remain intercalated with no net ion movement. In Figure 1.3(b,d), for sodium ions initially placed in the amorphous domain we observe intermediate mobility while remaining in the amorphous domain.

The explanation for the difference in the behavior of the lithium and sodium ions can be traced to the energetics. In Figure 1.4(b), the distributions of ion binding energies for the four sodium-containing composites are shown. The distribution again shifts to more favorable binding energies when loading is increased for sodium ions in either the crystalline or amorphous domain. This supports favorable ion-ion interactions. However, at both loading levels, the crystalline phase is significantly favored over the amorphous phase, which is in contrast to the behavior for lithium. The average sodium ion binding energies reported in Figure 1.5(b) bear out this observation: sodium ions prefer to reside in the crystalline phase. In these simulations, the sheet separation relaxes to energetically favorable distances. Sheet separation with fully intercalated sodium ions is 3.67 Å while sheet separations for other highly loaded systems are 3.20 ± 0.07 Å. There is no statistical difference between the two lithium cases because the initially intercalated lithium migrated out of the crystallite. The retention of sodium in the crystallite phase explains the increase in sheet separation. Since the crystallites are small and planar shifts occur often in disordered carbon composites, we do not believe that the sheet separation traps the sodium or otherwise influences sodium ions remaining intercalated.

Again, it is worth noting that these simulations cannot capture dynamic phenomena, which occur over timescales longer than the duration of the simulation. While the ion energies reveal that the crystalline phase is more stable, it remains unclear if the sodium ions initially placed in the amorphous domain would be able to intercalate within the crystallite. In bulk graphite systems, the intercalation of sodium is not observed unless Na-ions are solvated [70]. The barrier to intercalating sodium in bulk graphite is relatively high as stated by Okamoto *et al.* [54], due to a higher redox potential of Na/Na+, which would result in precipitation of Na metal rather than intercalation of the ion. It has been shown that graphitic nanocrystallites possess much greater flexibility and disorder than bulk graphite [69]. Thus, the feasibility of intercalation in these systems remains unknown.

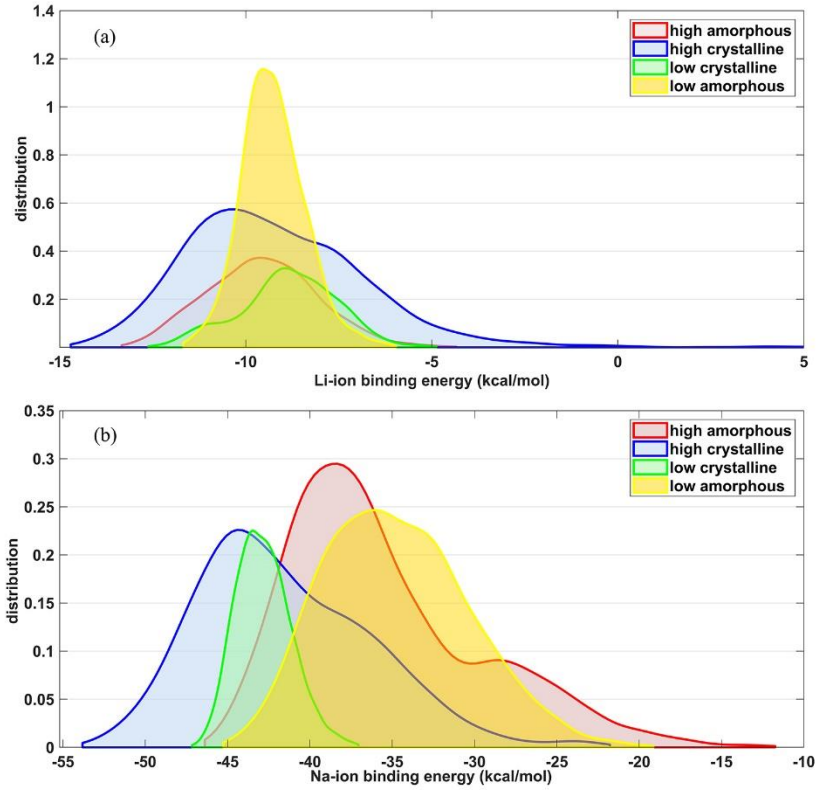


**Figure 1.4:** Distributions of ion binding energies in the simulated carbon composites charged with (a) lithium and (b) sodium ions.

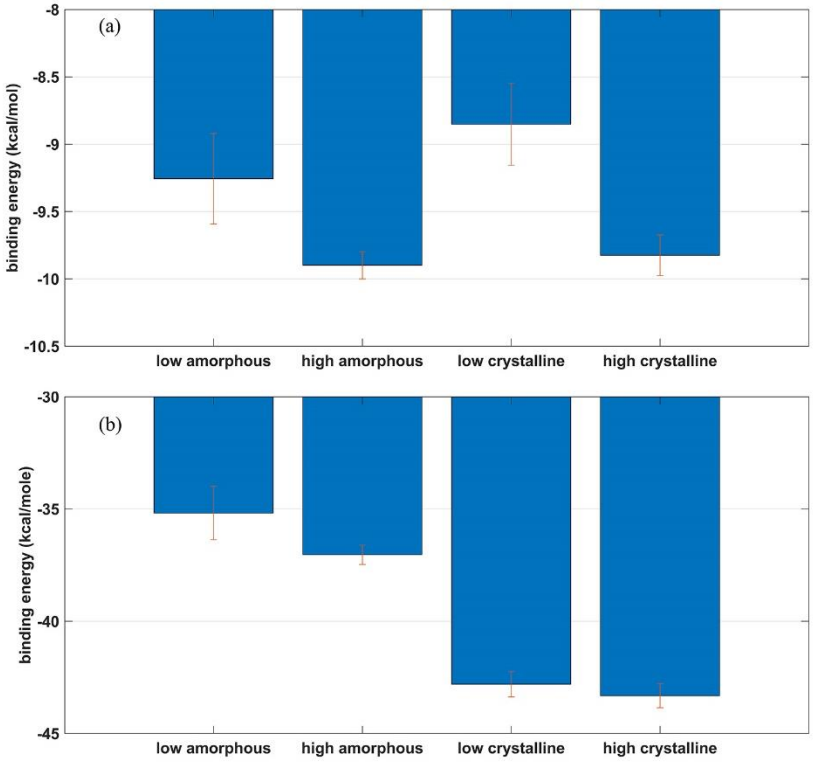


**Figure 1.5:** Average values and standard errors of the ion binding energies in the simulated carbon composites charged with (a) lithium and (b) sodium ions.

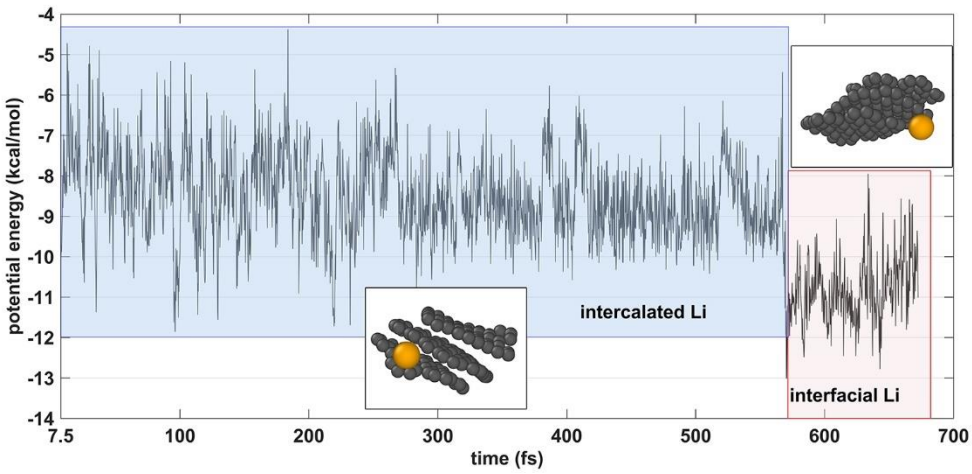


**Figure 1.6:** Potential energy as a function of time for the low loading (single ion) lithium-charged composite in which the lithium ion is initially placed in the crystalline domain. During this simulation, the ion can be observed to leave the crystallite resulting in a significantly more favourable binding energy.

***Metal and metal hydrides***

The same ReaxFF potentials used to simulate lithium and sodium ions in the charged carbon composite can also be used to simulate the metal hydrides. Lithium and sodium metals were also simulated to provide reference values for these ReaxFF interaction potentials. In Table 1.1, the minimized (0 K) lattice parameters from ReaxFF simulations experimental literature, and the energy per ion at 300 K are reported. The experimental lattice parameters for lithium and sodium metal were measured at 20 K while hydride systems were measured at 300 K [71,72]. Lattice parameter values for lithium systems are in good agreement with the literature while lattice parameters for sodium systems were underestimated by 3–5%.

The energy per metal atom or metal ion is relevant because they provide useful insight into the thermodynamic driving force for the distribution of lithium and sodium in the carbon composite. In the case of lithium, the metal hydride is the low energy state. Compared with the average ion energies in Figure 1.5(a), the hydride is more stable than the lithium ion in either the crystalline or amorphous domain. Using a pattern recognition approach, McNutt et al. showed that the archetypal structure for the most strongly bound lithium in the carbon forms a pattern as shown in Figure 1.7(a) [30]. In this figure, there is a lithium ion at the center of a cube with lithium nuclear density (green clouds) at the corners of the cube and hydrogen nuclear density (white clouds) in the faces of the cube. To be clear, nowhere is a structure like this observed because the hydrogen atoms are only present to terminate graphene sheets in either the crystalline or amorphous domain. The hydrogen atoms are tethered in place to a disordered matrix. However, averaging over all tightly bound lithium ions revealed this average structure. In retrospect, this is similar to the structure of the lithium hydride, which possesses an fcc structure of the NaCl type, as shown in Figure 1.7(b). However, the observed pattern found in the simulations differs by a rotation of 45° of the central four hydrogen locations. Thus, the extreme energetic favorability of the lithium hydride provides a thermodynamic driving force to place lithium at the interface between the crystalline and amorphous domains, where hydrogen is present rather than intercalated in the interior of a crystallite. This argument also supports the notion of lithium aggregation resulting in more stable binding energies with increased loading. McNutt et al. pointed out that the lithium storage mechanism in these carbon composites is therefore a different mechanism than storage in graphite. As such, lithium binding in carbon is not limited to the theoretical capacity of graphite and can explain the observed fact of storage above the limit of 372 mAh $g^{-1}$ [18].

An analogous comparison of the sodium metal and metal hydride energies in Table 1.1 with the ion energies in the carbon composite in Figure 1.5(b) for the sodium case reveals that sodium is energetically most stable in the carbon composite. Therefore, we do not observe the migration of the sodium to the hydrogen-rich interface.

The ReaxFF potential allows for charge redistribution during the simulation. In Table 1.2, the average lithium, sodium and hydrogen charges from simulations in the carbon composites and hydride phases are reported. These charges shed light on an important difference between the hydrides and the aggregates in the carbon composites. In the hydride, because hydrogen is more electronegative than either lithium or sodium, the hydrogen takes on a negative charge. However, in the composites, carbon is more electronegative than any other element in the simulation. Thus, the carbon takes on a negative charge and the lithium/sodium and hydrogen take on positive charges. This redistribution of charge does not negate the argument that the driving force of the hydride stability can explain the distributions of lithium and sodium in the composite. However, it does indicate that the carbon to which the hydrogen atoms are tethered plays a non-negligible role in the charge distribution.

In Figure 1.8, radial distribution functions (RDFs) describing the lithium–lithium and sodium–sodium distribution in the composites with high ion loading are shown. The RDF describes the local atomic structure and is proportional to the conditional probability of finding another ion at a given separation given that an ion sits at the origin. The noise in the RDFs is a consequence of the small system size. Larger simulations can provide much smoother RDFs out to longer separations. In the simulations with initial conditions in the crystalline domain, there is more structure in the sodium ions than in the lithium ions since they remain intercalated and their spacing is dictated by the graphitic structure. In the simulation with ions initially in the amorphous domain, we again observe more structure with the sodium ions. This is confirmed by the integration of the RDFs in Figure 1.8. At r distance 4.5 Å, the coordination numbers of sodium and lithium are 3.50 and 1.62 for initial placement in the crystallite, and 0.42 and 0.13 for sodium and lithium initially in the amorphous phase. The elucidation of the nature of this structure requires much larger scale simulations. Whether this structure is connected to sodium metal precipitation remains an open question.

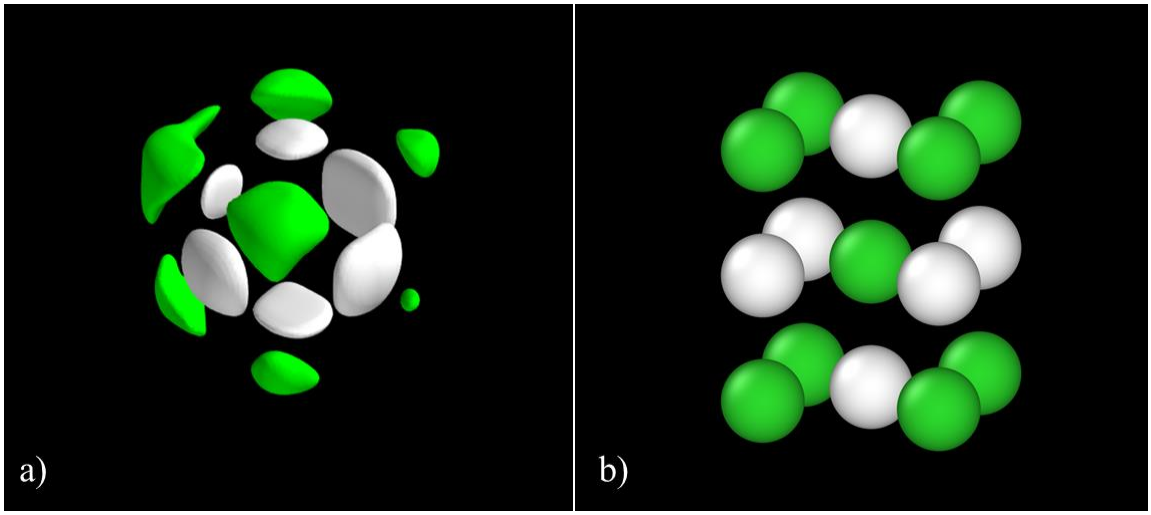


**Figure 1.7:** (a) Nuclear density distributions of lithium (green) and hydrogen (white) about a central lithium ion for tightly bound lithium in lignin-based carbon composite [30] (b) Lithium hydride structure shown for comparison.

**Table 1.1**: Lattice parameters and ion or atom energy for lithium and sodium in the metal and metal hydride phases.

| System (crystal structure) | Lattice parameter (Å) ReaxFF | Lattice parameter (Å) Experimental | Ion/atom energy (kcal/mole) |
|---|---|---|---|
| Lithium metal (bcc) | 3.429 | 3.478 [33] | -36.62 +/- 0.01 |
| Lithium hydride (fcc-NaCl type) | 4.065 | 4.084 [32] | -38.65 +/- 0.10 |
| Sodium metal (bcc) | 4.099 | 4.221 [33] | -21.19 +/- 0.01 |
| Sodium hydride (fcc-NaCl type) | 4.636 | 4.890 [32] | -33.57 +/- 0.01 |

**Table 1.2**: Lithium, sodium and hydrogen charges from simulations in the carbon composites and hydride phases.

| Material | Ion | Loading | Phase | Li/Na charge (e) | H charge (e) |
|---|---|---|---|---|---|
| composite | lithium | high | amorphous | 0.29 | 0.12 |
| composite | lithium | high | crystalline | 0.29 | 0.12 |
| composite | sodium | high | amorphous | 0.37 | 0.12 |
| composite | sodium | high | crystalline | 0.4 | 0.12 |
| hydride | lithium | N.A. | N.A. | 0.19 | -0.19 |
| hydride | sodium | N.A. | N.A. | 0.12 | -0.12 |

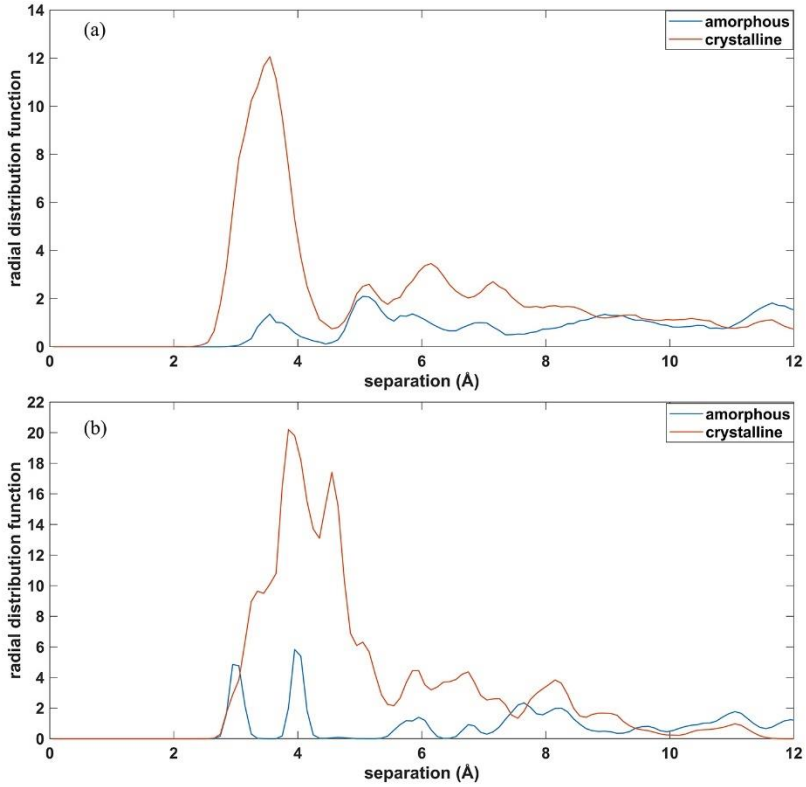


**Figure 1.8:** Radial distributions functions for (a) lithium–lithium and (b) sodium–sodium in the high loading simulations of the carbon composite initialized with ions in either the crystalline or amorphous domains.

## Conclusions

Reactive molecular dynamics simulations were performed for small systems of lithium and sodium ions in a model of lignin-based carbon composites. A classical simulation is an appropriate technique for this study because of the number of atoms required to model even a single graphitic nanocrystallite distributed in the amorphous carbon domain. In lithiated systems, these simulations clearly demonstrate a preference for binding at the interface of the crystalline and amorphous domains, where terminating hydrogen is present. Simulations of the metal hydride reveal that the most tightly bound lithium ions are moving towards a lithium hydride-like structure but are prevented from realizing this structure by the fact that the hydrogen is tethered to the relatively immobile carbon matrix. In the case of sodium, a very different result is observed. The energetically most stable state is the intercalated state although sodium ions in the amorphous phase exhibit binding energy that is more favorable than either the metal or the metal hydride. Large-scale simulations of the sodiated carbon composites with varying structures dictated by the processing conditions used to generate the composite are under way.

# CHAPTER II

## Lithium and Sodium Ion Binding Mechanisms and Diffusion Rates in Lignin-Based Hard Carbon Models

A version of this chapter is prepared for publication by by Dayton G. Kizzire, Alexander M. Richter, David P. Harper, and David J. Keffer

Kizzire, D. G., Richter, A. M., Harper, D. P. & Keffer, D. J. Lithium and Sodium Ion Binding Mechanisms and Diffusion Rates in Lignin-Based Hard Carbon Models

The following article's content is unchanged from the above publication except for format. The publication is two-column format and below the article is in single-column format. The numbers in the section headings have also been removed. Figure and Table positions have been moved slightly to accommodate the required format.

Credit authorship contribution statement:
Dayton G. Kizzire: Investigation, computational resource acquisition, simulations, formal analysis, writing (original draft), data visualization, data curation. Alexander M. Richter: simulations, data visualization, computational resource acquisition. David P. Harper: Writing – review & editing. David J. Keffer: Conceptualization, methodology, computational resource acquisition, supervision, formal analysis, investigation, Writing – review & editing.


## Abstract

Hard carbons are the primary candidate for the anode of next generation sodium-ion batteries for large-scale energy storage as they are sustainable and can possess high charge capacity and long cycle life. These properties along with diffusion rates and ion storage mechanisms are highly dependent on nanostructure. This work uses reactive molecular dynamics simulations to examine lithium and sodium ion storage mechanisms and diffusion in lignin-based hard carbon model systems with varying nanostructure. It was found that sodium will preferentially localize on the surface of curved graphene fragments while lithium will preferentially bind to the hydrogen dense interfaces of crystalline and amorphous carbon domains. The ion storage mechanisms are explained through ion charge and energy distributions in coordination with snapshots of the simulated systems. It was also revealed that hard carbons with small crystalline volume fractions and moderately sized sheets of curved graphene will yield the highest sodium-ion diffusion rates at ~$10^{-7}$ $cm^2/s$. Self-diffusion coefficients were determined by mean square displacement of ions in the models with extension through confined random walk theory.

## Introduction

Efficient, sustainable, and low-cost energy storage is a global necessity. For the past 30 years, Li-ion batteries have been the gold standard and workhorse of energy storage needs for mobile electronics, electric vehicles, medical devices, *etc.*; however, lithium is not an infinite resource and its storage in earth's crust is localized to a few countries. Since this is the case, researchers have been exploring options for the replacement of lithium as the charge carrying ion in energy storage devices with sodium as one of the most promising options as it is low-cost, has similar insertion chemistry, is widely globally available, and can be used in cost and weight prohibitive situations like large-scale grid support and stationary energy storage for renewable energy sources [73-75].

One of the primary challenges of replacing lithium with sodium in current energy storage devices deals with the inability for sodium to intercalate within graphite and form binary graphite intercalation compounds or b-GICs with any reasonable charge density [67,76]. It has been shown previously that sodium will only form $NaC_{64}$ when inserted into graphite [77]. This has led researchers to exploring hard carbons as anode materials. Depending on nanostructure, hard carbons have the potential to possess a greater charge density, higher resistance to degradation from electrolyte interactions, low working voltage, longer cycle life, and a higher degree of sustainability when compared to the current commercial flake-graphite and spherical graphite (SPG) anodes [67,78,79].

Recent research has suggested lignin as a sustainable and domestic source for nanostructured hard carbons with far reaching applications in energy storage [13,18,58,80]. Lignin is a highly abundant and renewable resource that possesses high carbon content and an amorphous, cross-linked three-dimensional structure of aromatic polymers [81,82]. Defining a complete processing-structure-property-performance (PSPP) relationship between lignin and carbonaceous products is difficult since lignin is derived from woody plants and grasses and the relative fractions of the constituent organic compounds are highly variable by feedstock which in turn influences the nanostructures and properties of the final carbon composites [21]. Research into the PSPP relationships of lignin reveals that pyrolizing and reducing lignin produces hard carbon composites composed of an amorphous matrix with embedded crystalline domains. The crystalline volume fraction (CVF), crystallite size, and crystallite form (spheres, fullerenes, onion-fullerenes, nanotubes, multiwalled nanotubes, graphite, etc.) of lignin based hard carbons can be tuned via the choice of lignin feedstock, processing, and carbonization temperature [21,62,83]. The work of García-Negrón *et al.* demonstrates that pyrolizing, reducing at 1050 °C, and ball milling of kraft softwood lignin produces a carbon composite material composed of spherical nanocrystallites embedded in an amorphous graphene matrix which, when processed into an anode and tested in a Li-ion coin cell battery, possesses a specific capacity of 444 mAh/g with 98% coulombic efficiency over extended galvanostatic cycles

[18]. This shows that lignin-based carbon composites (LBCCs) can achieve at least a 20% increase in specific capacity over traditional graphitic anodes (372 mAh/g) and can be considered as a high efficiency, sustainable, and low-cost option for battery electrodes.

Present challenges facing researchers with hard carbon electrodes lie in understanding the ion storage mechanisms, preferential ion localization, volume change (swelling) during (de)sodiation and (de)lithiation, as well as the optimal nanostructure-porosity-density-CVF combination to achieve the highest performance [67,84]. To investigate solutions to some of these challenges for LBCCs, McNutt *et al.* created large scale models of the LBCCs with varying crystallite sizes, crystalline volume fractions, and densities to emulate the LBCCs synthesized at different reduction temperatures from hardwood lignin [30]. Molecular dynamic simulations of the LBCC models charged with lithium revealed that the carbon-edge-terminating hydrogen play a critical role in the ion storage mechanism for LBCCs as Li-ions preferentially localize in the hydrogen dense interfacial region between crystallites and amorphous graphene fragments and allows Li-ions to be stored at a greater density than when intercalated between planes of graphite as $LiC_6$ [19,20]. McNutt *et al.* also explains that as crystallite size decreases, interfacial volume and hydrogen content increases leading to larger Li-ion storage capacity [20]. To further explain the ion storage mechanism in LBCCs, Kizzire *et al.* used a small subsystem of the McNutt *et al.* composites that consisted of a single nanocrystallite embedded in a matrix of amorphous graphene fragments and simulated with lithium and sodium loading configurations using ReaxFF potentials [85]. Reactive potentials consume more computational resources than non-reactive potentials; however, they allow modelling of the formation and dissociation of chemical bonds and include both the coulombic interactions and van der Waals forces necessary for accurate modelling of charged graphitic anodes [51,52,85,86]. The ReaxFF potentials were deemed necessary as accurately capturing the charge transfer between ions and host structure is critical to understanding ion migration and preferential ion localization [85]. Kizzire *et al.* revealed that sodium, if not initially placed in an intercalated site, will preferentially localize in the amorphous graphene region whereas lithium will migrate from both intercalated and amorphous graphene initial positions to the hydrogen dense interfacial regions and attempt to form a lithium hydride like structure but are incapable as the hydrogen are tethered to the relatively immobile carbon matrix [85]. Results from this previous study prompted interest into investigating lithium and sodium in large-scale LBCC models with ReaxFF potentials.

For application purposes, knowledge of diffusion rates and ion migration are critical to understanding the performance of an anode material. The self-diffusion coefficient is obtained by using the Einstein relation and calculating a single-particle autocorrelation function, the mean square displacement (MSD). The Einstein relation includes the condition that the MSD is linearly proportional to observation time, which occurs in the

infinite-time limit. Simulating confined systems that operate with short time scales (1 ns) often do not meet this condition, and thus, application of the Einstein relation is not valid [87]. A robust solution to this issue is shown by Calvo-Muñoz *et al.* where the MSD of MD simulations can be extended to reach the infinite-time limit by fitting the MSD of a confined random walk (CRW) simulation to the MSD from the MD simulation [87]. The confined random walk theory uses two physical parameters, cage radius and cage-to-cage hopping probability. These parameters represent the physical system's dimensions and the activation barrier for diffusion respectively, ensuring an accurate result for the self-diffusion coefficient. The work below uses the same CRW simulation code as Calvo-Muñoz *et al.* to obtain self-diffusion coefficients for lithium and sodium in the LBCC anodes.

This work builds upon the previous work of McNutt *et al.* and Kizzire *et al.* and investigates lithium and sodium in large-scale LBCC models with reactive potentials to determine preferential localization, composite swelling, mesoscale interactions, and lithium/sodium diffusion rates. We accomplish this by analyzing the resulting radial distribution functions (RDFs), charge and energy distributions, mean square displacement of lithium and sodium ions extended by confined random walk theory, and snapshots of charged composites. This work is propelled by interest in using LBCCs as sustainable, domestic, and low-cost electrodes for sodium and lithium-ion batteries. In this study, an array of lithium and sodium loading configurations in three carbon composites of 90, 50, and 10% crystalline volume fraction were designed to emulate the hardwood-lignin based carbon composites synthesized by Tenhaeff *et al.* [13].

## Methods

The hard carbon models in this work were designed by McNutt *et al.* to emulate the nanostructure of hardwood lignin pyrolyzed and reduced at 1000, 1500, and 2000 °C as synthesized and characterized by Tenhaeff *et al.* [13,30]. The hard carbon models possess spherical AB stacked graphite crystallites with radii of 5, 7, and 17 Å embedded in an amorphous graphene fragment matrix at 90, 50, and 10% crystalline volume fractions, respectively. All crystalline and amorphous edge carbons were terminated with hydrogen. Relaxation of the model resulted in slight bending of the graphene fragments in the amorphous domain and shifts in crystalline planes such that the equilibrium interplanar spacing became 3.4 Å, representative of the disorder in the real LBCC system and verified as accurate by comparison of the simulated and experimental RDFs [30].

A total of nine reactive simulations (three without ion loading, six with ion loading) were performed using LAMMPS and with ReaxFF potentials developed by Hjertenæs *et al.* and Raju *et al.* for the sodiated and lithiated systems respectively [51,68,88]. Previous works

have verified that the two reactive potentials are the same in their handling of carbon-carbon and carbon-hydrogen interactions, and thus, the Raju *et al.* potential was used for the systems without ions [85]. The nine systems were relaxed at 1 atm in the NPT ensemble at 298 K with 0.25 fs timestep until potential energy was equilibrated. The six systems with lithium/sodium loading were then simulated for 1 ns in the NVT ensemble at 298 K with 0.25 fs timestep. The trajectory files were saved in both wrapped and unwrapped configurations for the RDF and MSD analysis, respectively and the volume of each system was recorded for swelling calculations. The charge densities for Na-ion systems were set between 100-125 mAh/g, consistent with values used in previous work for these composite systems [19]. The differing charge density between sodium and lithium systems is due to the difference in ion mass, as all 50% CVF systems have the same number of ions.

Ideally, the results of a simulation are independent of initial ion placement when the simulation is run a sufficiently long time to drive the system to thermodynamic equilibrium. However, the finite simulation time and kinetic barriers result in systems with distinct initial conditions, such as ions initially placed in the graphitic versus amorphous domains, not arriving at the same state. This was investigated by McNutt for lithium [20]. Since the energy was lower for the amorphous system, he judged that it was the more energetically probable state. Based on this result, in the simulation matrix implemented in this present work, some of the composites are investigated with initial placement of ions in both the crystalline and amorphous domains, while others are investigated exclusively with ions initially placed in the amorphous domain.

The 90 and 10% CVF systems were simulated uncharged and with sodium initialized in the amorphous carbon domain. The 50% CVF system was simulated uncharged, with sodium and lithium initialized in intercalated positions within the crystalline carbon domain, and with sodium and lithium initialized in the amorphous carbon domain. The 90% CVF system contained 155,964 atoms (88,447 crystalline carbon, 8,835 amorphous carbon, 53,668 hydrogen, and 5,014 sodium). The 50% CVF system contained 113,160 atoms (49,232 crystalline carbon, 26,563 amorphous carbon, 32,353 hydrogen, and 5,012 lithium/sodium). The 10% CVF system contained 689,788 atoms (423,744 crystalline carbon, 131,915 amorphous carbon, 102,814 hydrogen, and 31,278 sodium). The large number of atoms in each system are necessary to capture both the mesoscale structure of LBCC anodes and an accurate crystalline volume fraction with appropriately sized crystallites. These model structures have been extensively compared to synthesized carbon composites [30]. A full table of system details can be found in Table 2.1.

**Table 2.1:** Collection of simulated systems with relevant parameters.

| System | Crystalline Volume Percentage | Number of atoms | Initial Ion Placement | Charge Density (mAh/g) | Composite Density (g/cm3) | Crystallite Radius (Å) | Swelling Percentage |
|---|---|---|---|---|---|---|---|
| 1 | 10 | 658,510 | None | 0 | 1.68 | 17 | - |
| 2 | 10 | 689,788 | Na - Amorphous | 111.82 | 1.60 | 17 | 15.6 |
| 3 | 50 | 108,148 | None | 0 | 1.62 | 7 | - |
| 4 | 50 | 113,160 | Li - Intercalated | 137.44 | 1.53 | 7 | 10.0 |
| 5 | 50 | 113,160 | Li - Amorphous | 137.44 | 1.54 | 7 | 8.7 |
| 6 | 50 | 113,160 | Na - Intercalated | 126.99 | 1.60 | 7 | 13.3 |
| 7 | 50 | 113,160 | Na - Amorphous | 126.99 | 1.57 | 7 | 15.8 |
| 8 | 90 | 150,950 | None | 0 | 1.54 | 5 | - |
| 9 | 90 | 155,964 | Na - Amorphous | 100.45 | 1.49 | 5 | 12.9 |

## Results and Discussion

### *Ion Charge and Binding Energy Analysis*

In the following section we compare the energy and charge distributions for the LBCC models with lithium and sodium loading configurations. Figure 2.1 shows the binding energy and charge distributions for lithium and sodium ions in the intercalated and amorphous initial loading configurations for the 50% CVF system. Examining the Li-ion binding energy and charge distributions in Figure 2.1, we can see that after simulating for 1 ns, the respective distributions are nearly identical for both the amorphous and crystalline intercalated initial loading configurations. This result informs us that the Li-ions will migrate to the hydrogen dense interfacial regions irrelevant of the initial position, and denotes that interfacial regions are the most preferable binding site for Li-ions in these LBCC hard carbon anodes, which is in good agreement with previous works [20,85].

Examining the Na-ion binding energy and charge distributions in Figure 2.1 for the 50% CVF system simulated for 1 ns, we can see a single mode distribution for Na-ions intercalated in the crystallites and a distinct bimodal distribution for Na-ions initialized in the amorphous domain. Through searching ions in snapshots of the simulation frames and identifying their charges and binding energies, we found that Na-ions sandwiched between neighboring planes of amorphous graphene fragments had similar binding energies and charges to those Na-ions that were intercalated within the crystalline domain. These "doubly bound" Na-ions had deeper binding energies and higher charges compared to the Na-ions that adsorbed onto the planar surfaces of amorphous graphene fragments and crystallites. These distributions also show that the hydrogen in the system do not exhibit the same driving force effect on Na-ions to pull them into interfacial regions as they do with the Li-ions.

Figure 2.2(a-b) shows the binding energy and charge distributions after 1 ns of simulation for Na-ions initialized in the amorphous graphene domain for the 10, 50, and 90% CVF systems. Inspection of Figure 2.2(a-b) shows a large percentage of Na-ions having deeper binding energy and greater charge in the 90% CVF system compared to the 10 and 50% CVF systems. Na-ions with binding energies that average -37 kcal/mol in the 90% CVF system correlates to Na-ions that are sandwiched between adjacent graphene planes or Na-ions at intercalation positions at the edge of nanocrystallites with high amounts of disorder in interplanar spacing and angles. Na-ions with binding energies near -20 kcal/mol are found adsorbed onto a graphene surface or a basal plane of a nanocrystallite. The greater percentage of Na-ions with deeper binding energy in the 90% CVF system results from the high fraction of graphene planes directly adjacent to crystallites or each other which decreases the amount of adsorption sites. The lower crystalline volume fraction systems allow a more even distribution between these two Na-ion localizations.

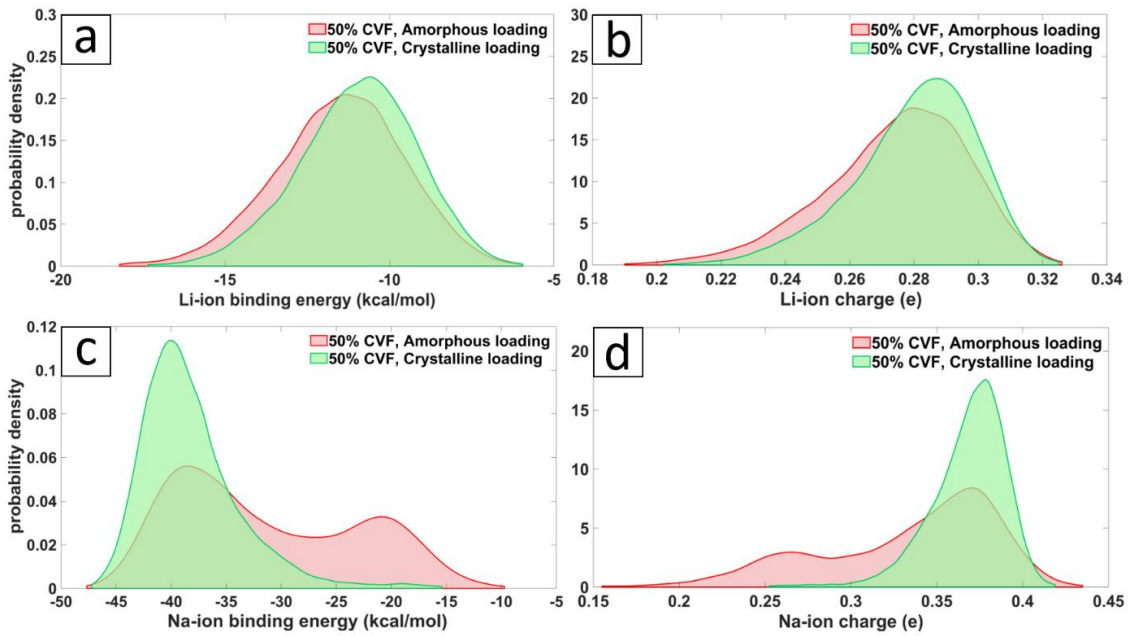


**Figure 2.1:** Binding energy and charge distributions for lithium (a-b) and sodium (c-d) in the 50% crystalline volume fraction system for ions initialized in the amorphous and crystalline domains.

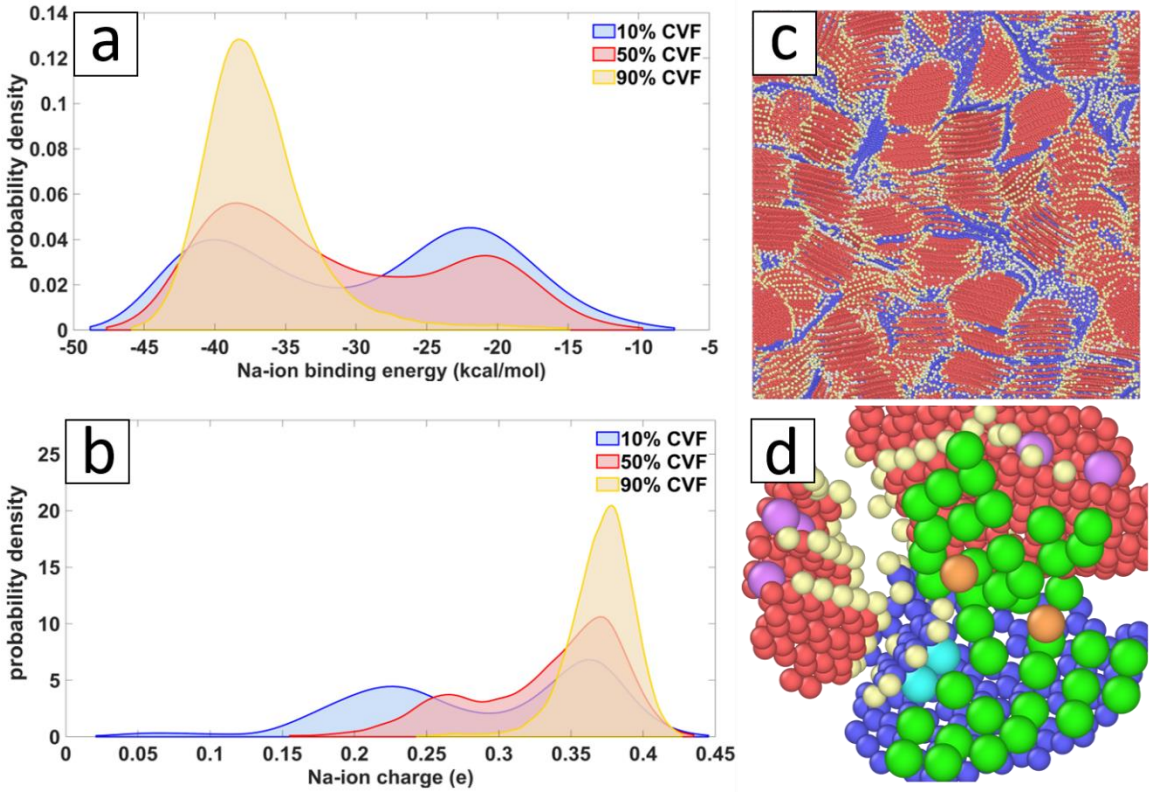


**Figure 2.2:** (a-b) Binding energy and charge distribution for sodium initialized in the amorphous domain for the 10, 50, and 90% CVF systems. (c) Front facing view of the sodiated 10% CVF system with crystalline carbon (red), amorphous graphene fragments (blue), sodium (white), and hydrogen (removed for clarity). (d) An enlarged section of the 10% CVF system with sodium color coded to represent charge and binding location. Na-ions bound to the surface of graphene and crystallites (green), Na-ions intercalated between neighboring sheets of graphene (light blue), Na-ions intercalated within edges of nanocrystallites (purple), and Na-ions bound to other Na-ions in a semi-metallic like state (orange).

Interestingly, the charge distribution for Na-ions in the 10% system show a third state of Na-ion charge, centered at 0.06 e, not present in other systems. To identify the source of this third state of Na-ion charge we look to the Figure 2.2(d) which presents a zoomed section of Figure 2.2(c) with Na-ions color coded to correspond to charge value. Light blue and purple represent doubly bound Na-ions in the amorphous (blue) and crystalline (red) domains respectively with an average charge value of 0.36 e. Light green represents the Na-ions adsorbed (or singly bound) to the surface of an amorphous or crystalline carbon plane with an average charge value of 0.225 e while orange represents the third localization only found in the 10% CVF system with an average charge value of 0.06 e and low average binding energy of 14 kcal/mol. These orange Na-ions are bound to each other and the low charge represents a quasi-metallic like state. Higher loadings of Na-ions in these moderately porous composites would create more Na-ion clustering within the pores, similar to the orange-colored ions in Figure 2.2(d). Na-ion clustering inside pores has been reported by others in the literature as stable configurations that have been shown to be highly reversible and enable charge densities near 300 mAh/g in hard carbon anodes [84,89].

Through examination of Figure 2.2(a, d) we can see that most Na-ions in the 10% CVF system are adsorbed onto the face of a graphene fragment. Further, even though the sodium were initialized randomly throughout the composite, there are obvious regions in the amorphous graphene domain with higher and lower concentrations of sodium, suggesting that in these low CVF composite systems, sodium will preferentially aggregate.

While the binding energy distributions in Figure 2.1 show that intercalation positions are more energetically favorable for sodium, the barrier for Na-ion intercalation is very high, as reported in the literature [47,67,76]. This is true except for the case where nanocrystallite planes have shifted, and Na-ions intercalate along the crystallite edges where interplanar distance is larger than 3.6 Å, as seen with the Na-ions colored purple in Figure 2.2(d). Analysis of the energy and charge distributions in conjunction with the snapshots suggest that in application, sodium insertion into LBCC anodes would result in Na-ions preferentially adsorbing to the surface of amorphous graphene fragments and the surface planes of nanocrystallites with a small fraction intercalating along the edges of nanocrystallites where local interplanar spacing is above 3.6 Å due to inherent disorder in the system. Inspection of Figure 2.2(b,d) implies that after the preferential filling of adsorption and intercalation storage sites, sodium will fill porous regions in the composite. Qualitatively speaking, from these results it is reasonable that lower crystalline volume fraction combined with smaller nanocrystallites and moderate porosity would allow the highest energy density for sodiated LBCC anodes. For specific application where power density or fast charging is paramount, interconnectivity of pores would allow more rapid movement of sodium through the LBCC anode. Recent DFT studies of alkali metals in

hard carbon anodes by Olssen *et al.* substantiate this claim with findings which state that large, curved graphene sheets as part of pore structure aids in rapid ion diffusion and the weaker binding energies of ion to graphene contribute to higher cycling performance [77]. It should be mentioned that Olssen *et al.* defines a pore structure as a space of at least 6.5 Å between planes of graphene [77]. For the context of this work, pores should be defined as an open space between graphene planes or nanocrystallites with spacing from 6.5 Å to multiple nanometers.

For glucose based hard carbons, Au *et al.* found that pores were highly interconnected at carbonization temperatures of 1000 °C and while pores were larger for carbonization at 2000 °C, the increasing size of the graphitic regions closed off the interconnected pore structures leading to isolated pores [90]. It is reasonable that porosity in LBCCs would progress in a similar manner, suggesting lower reduction temperatures will create interconnected pores yielding high sodium mobility throughout the composite while slightly higher reduction temperatures will yield larger pores allowing a greater sodium storage capacity through the adsorption-intercalation-pore filling sodiation scheme.

### *Anode Swelling*

In application, knowledge of the volume change that occurs in an anode during ion (de)loading is vitally important as excessive volume change can damage battery structure leading to failure with safety concerns. In general, the volume change between empty and fully intercalated graphitic anodes in commercial Li-ion batteries is $\leq$ 10 - 14% [91,92]. The swelling for each of the LBCC simulated systems can be found in Table 2.1. We can see that lithium initialized in the amorphous domain produces the least amount of swelling, which is to be expected since lithium preferentially localize in the interfacial regions, bound to hydrogen at a greater density than when intercalated in graphite [19,20,85]. LBCCs loaded with sodium exhibit roughly 50% greater swelling than composites loaded with lithium. This is also expected as sodium has a greater ionic radius and does not exhibit the same high-density binding with hydrogen as lithium. We note that these swelling values were obtained from simulating at atmospheric pressure and anode structure could isotropically expand, whereas in application, the anode structure is constrained within the battery housing. Additionally, the Li-ion charge density in these simulated systems is approximately one third that of fully Li-intercalated graphite since the charge density was chosen to correspond to charge density in previous works as stated in the methods section. Reporting of these swelling values are meant to provide reference for future experimental endeavors in the creation and characterization of Li and Na-ion batteries with LBCC anodes.

***Local Structure Analysis***

In Figure 2.3(a-d) the ion-ion and ion-hydrogen radial distribution functions are shown for the 50% CVF system with amorphous and crystalline initial loading states. The Li-Li and Li-H RDFs found in Figure 3(a-b) are highly similar as both initial loading conditions result in Li-ions migrating to the hydrogen dense interfacial region as can be seen in the simulation cell slices in Figure 2.4(a-b). One would expect there to be more long-range structure in the Li-H PDF due to the Li-ions affinity for bonding to the hydrogen; however, since the hydrogen are essentially tethered to the relatively immobile carbon, no long-range Li-H structure can exist. The increased order found in the Na-H PDF for Na-ions shown in Figure 2.3(d) is only due to the favorable energy state they find when situated in the middle of the carbon rings on the surface of graphene and in intercalation positions. The dip occurring in the Na-Na PDF for intercalated Na-ions in Figure 2.3(c) near 9 Å denotes the average distance of a Na-ion to the interfacial region where no ions are present, and the subsequent rise near 11 Å is the average distance between Na-ions found between separate nanocrystallites as seen in Figure 2.4(d).

The Na-ion component RDFs for the various composites can be seen in Figure 2.5(a-d) along with visual representations of the ion-atom pairs that constitute each peak. The most notable among these RDFs is Figure 2.5(a) where the increased intensity in Na-Na pairs for the 10% CVF system denotes a greater local density of Na-ions suggesting an increased amount of agglomeration, as can be seen in Figure 2.6(a). Examination of Figure 2.5(a) and Figure 2.6(a-c) reveals an inverse relationship between crystalline volume fraction and local Na-ion density, with low crystalline volume fraction and moderate porosity displaying the highest degree of Na-ion agglomeration.

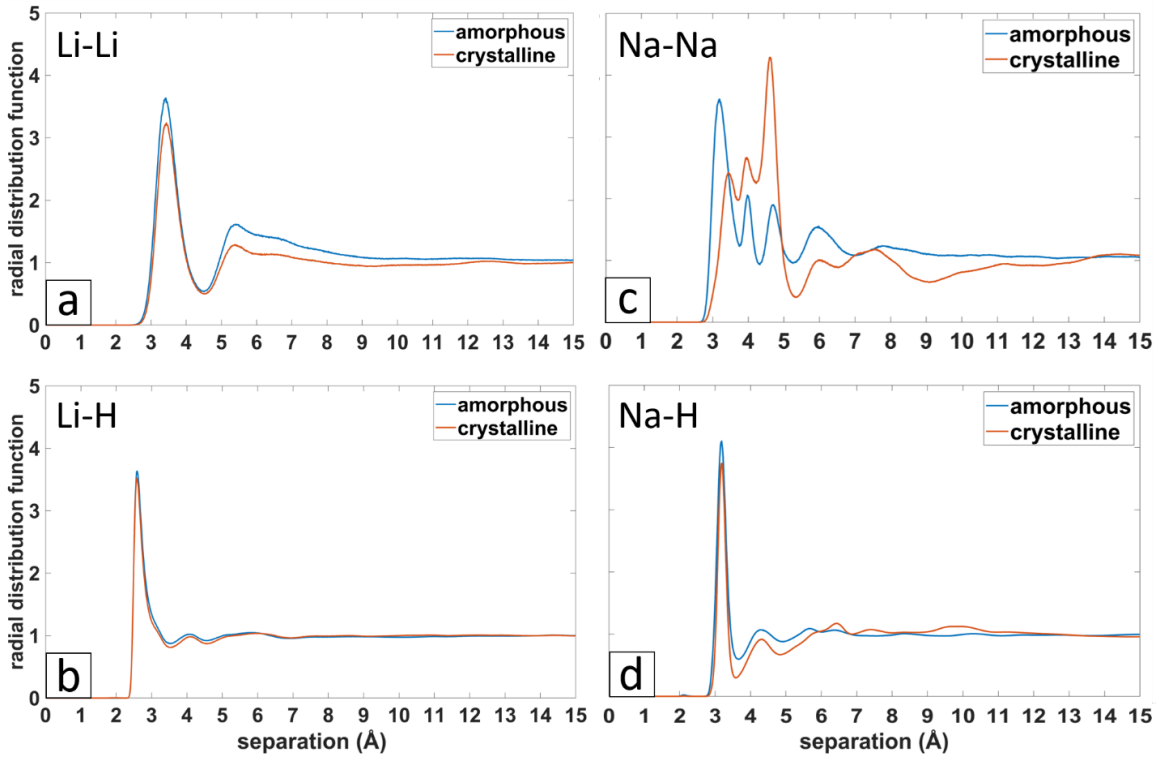


**Figure 2.3:** Component radial distribution functions for ions initialized in the amorphous graphene and crystalline intercalation domains for the 50% CVF system. (a) Li-Li PDF, (b) Li-H PDF, (c) Na-Na PDF, and (d) Na-H PDF.

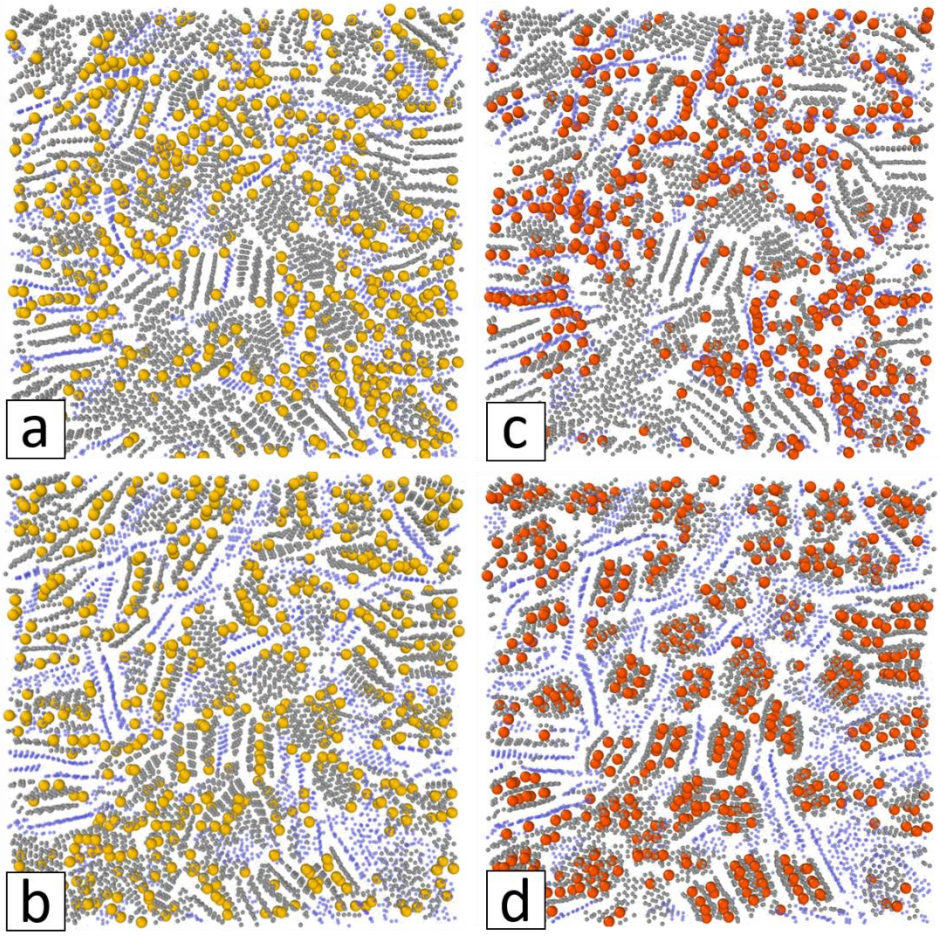


**Figure 2.4:** Snapshot slices of the 50% CVF systems after simulation for 1 ns with lithium (yellow), sodium (red), crystalline carbon (grey), amorphous carbon (blue), and hydrogen (removed for clarity) (a) lithium initialized within the amorphous domain, (b) lithium initialized as intercalated within the crystalline domains, (c) sodium initialized within the amorphous domain, (d) sodium initialized as intercalated within the crystalline domains.

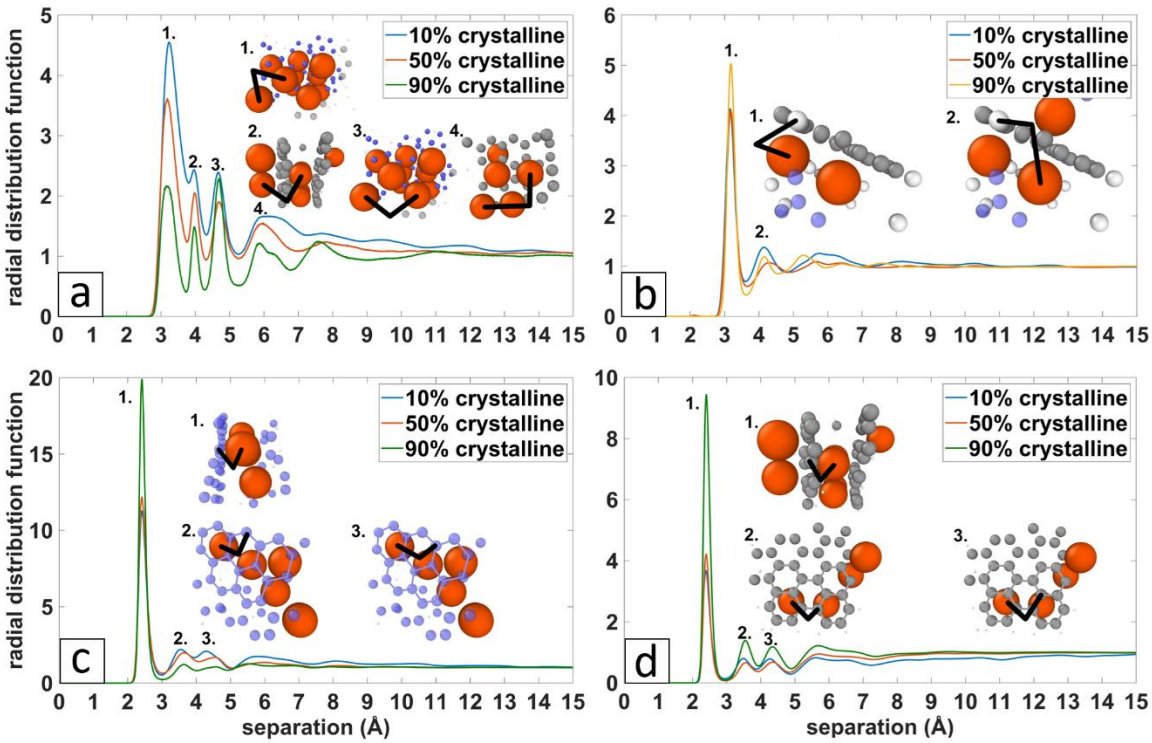


**Figure 2.5:** Na-atom component radial distribution functions for each of the amorphous sodiated LDCC systems with corresponding snapshots of the general Na-atom pairs representing each peak in the RDFs. (a) Na-Na RDFs, (b) Na-H RDFs, (c) Na-amorphous graphene RDFs, (d) Na-crystalline carbon RDFs.

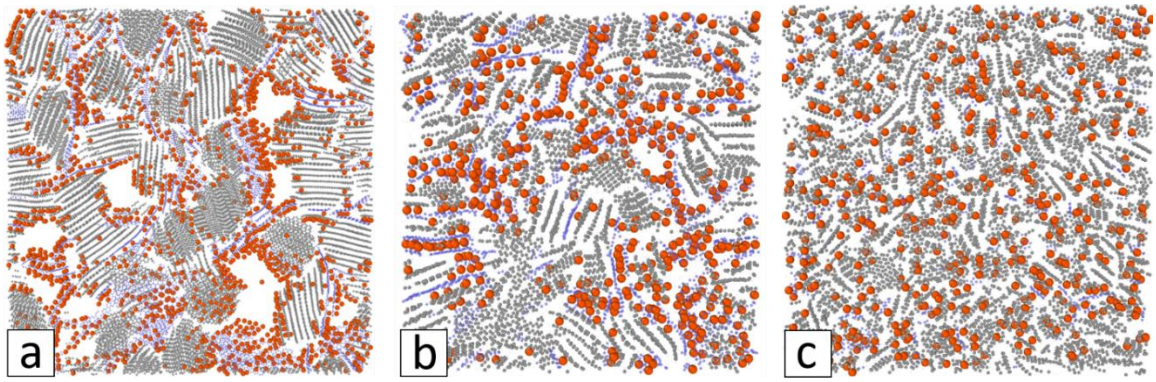


**Figure 2.6:** Snapshot slices of LDCC systems with sodium initialized in the amorphous domain for (a) 10% CVF, (b) 50% CVF, (c) 90% CVF.

### *Ion Diffusion*

To calculate the self-diffusion coefficients for lithium and sodium in the LBCC anodes, we recorded the unwrapped coordinates of ions during simulations and calculated the mean square displacement (MSD) of ions through the composites. The MD generated MSDs were then fit with the confined random walk (CRW) simulation at room temperature and extended to 100 ns. The cage radius and cage-to-cage hopping probability reported in Table 2.2 represent a characteristic length scale of confinement and a probability proportional to the activation barrier to ion diffusion respectively [87]. Where the cage radius is less than the diameter of an atom, this describes the relative volume explored by the point at the center of the ion. The exponent value details the linear proportionality of MSD to observation time, which is required by the Einstein relation. Table 2.2 reports the MSD values of MD simulation alone and with extension to the long-time limit (represented with an exponent value near 1.0) with CRW theory. The MSD from MD simulation are plotted with their corresponding CRW extensions up to 1 ns in Figure 2.7. We note that the CRW were simulated out to 100 ns but plotted to 1 ns for clarity in comparing with the MD simulations. The MSD data from MD simulation are plotted to 0.5 ns because auto correlation functions become noisy near the end since there is a decreasing amount of data in each subsequent point. Likewise, the calculations of diffusion coefficients from MD simulation only used data up to 0.5 ns. The self-diffusion coefficients were calculated using mean square displacement with extension through confined random walk theory to reach the long-time limit required by the Einstein relation.

We find the CRW values for the self-diffusion coefficients for lithium in the 50% CVF system and sodium in the 10% CVF system are on par with the experimentally found and ab initio calculated diffusion rate of lithium in pristine graphite in the planar direction, 4.4 x $10^{-7}$ $cm^2/s$ [93]. The CRW values of diffusion rate for sodium in the 50 and 90% CVF systems are slightly smaller with values ~$10^{-8}$ $cm^2/s$. Sodium in the 10% CVF system was found to have the highest diffusion rate of all simulated systems with a value of 2.8 x $10^{-7}$ $cm^2/s$ while sodium in the 90% CVF system was found to have the lowest diffusion rate among the systems studied. Ab initio simulations conducted by Koh *et al.* show that there is a strong correlation between sodium ion diffusion rate and the degree of curvature of graphene planes, where increasing curvature of graphene planes decreases the barrier for sodium migration on the concave size of the graphene plane [94]. Since the graphene planes in the 10% CVF are larger and possess a higher degree of curvature compared to the 50 and 90% CVF systems, the high diffusion rate of sodium in the low CVF system is substantiated.

**Table 2.2:** Mean square displacement values from MD experiment and CRW extension for charged composites.

| System | Ion - Initial Domain - CVF system | MD Exponent | CRW Exponent | MD Diffusion Coefficient ($cm^2/s$) | CRW Diffusion Coefficient ($cm^2/s$) | Cage Radius (Å) | Cage Hopping Probability |
|---|---|---|---|---|---|---|---|
| 2 | Na - Amorphous - 10 | 0.77 | 0.97 | $2.70 \times 10^{-7}$ | $2.76 \times 10^{-7}$ | 0.90 | 0.00141 |
| 4 | Li - Intercalated - 50 | 0.66 | 0.97 | $1.53 \times 10^{-7}$ | $1.63 \times 10^{-7}$ | 1.05 | 0.00067 |
| 5 | Li - Amorphous - 50 | 0.64 | 0.97 | $1.24 \times 10^{-7}$ | $1.27 \times 10^{-7}$ | 0.92 | 0.000617 |
| 6 | Na - Intercalated - 50 | 0.45 | 1.10 | $1.04 \times 10^{-8}$ | $1.43 \times 10^{-8}$ | 0.44 | 0.000134 |
| 7 | Na - Amorphous - 50 | 0.67 | 1.04 | $2.00 \times 10^{-8}$ | $2.29 \times 10^{-8}$ | 0.398 | 0.000275 |
| 9 | Na - Amorphous - 90 | 0.65 | 0.95 | $2.51 \times 10^{-8}$ | $2.62 \times 10^{-8}$ | 0.51 | 0.000252 |

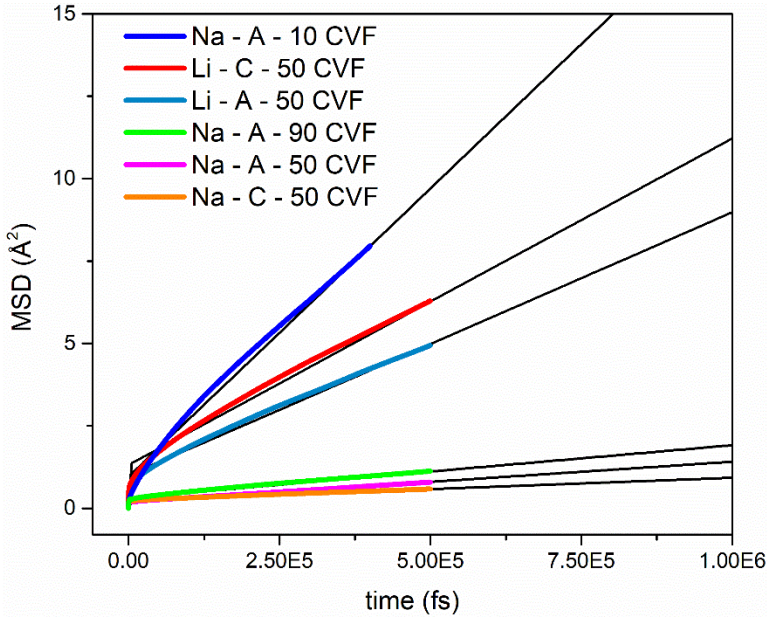


**Figure 2.7:** Mean square displacement generated from MD simulations (color) with their corresponding CRW extensions up to 1 ns.

## Conclusion

Reactive molecular dynamics simulations were carried out for lithium and sodium loaded in three large lignin-based-carbon-composite systems with 10, 50, and 90% crystalline volume fractions. The reactive potentials used for this work were deemed necessary to accurately capture the ion binding mechanisms, diffusion properties, and the complex mesoscale structure intrinsic to plant-based hard carbons. Analysis of energy and charge distributions in conjunction with snapshots of the lithiated systems shows lithium will preferentially localize in the hydrogen dense interfacial region between crystallites and amorphous graphene fragments regardless of initial localization.

Snapshots of the sodiated systems in conjunction with charge and energy distributions reveal that sodium will preferentially bind to the surface of graphene and basal surfaces of nanocrystallites with a small fraction intercalating at the edges of nanocrystallites that have local d-spacing above 3.6 Å due to the inherent disorder in the nanocrystallites. Once the adsorption and intercalation positions have been filled, sodium will agglomerate in pores. This adsorption-intercalation-pore filling sodiation scheme leads to high charge capacity in hard carbon anodes. The lower binding energies found for the adsorption and pore filling sodium ions also suggest these storage mechanisms to be largely reversible.

It was found that the LBCC system with the lowest crystalline volume fraction and curved graphene fragments along pores produces the largest sodium ion diffusion rate among the composites studied in this work. The results of this study indicate that a porous lignin derived carbon composite with low crystalline volume fraction and long sheets of curved graphene will produce an anode with high diffusion rate and large charge capacity for a sodium-ion battery.

# CHAPTER III

# Lithium and Sodium Ion Binding Mechanisms and Diffusion Rates in Lignin-Based Hard Carbon Models

A version of this chapter is prepared for publication by by Dayton G. Kizzire, David P. Harper, and David J. Keffer

Kizzire, D. G., Harper, D. P. & Keffer, D. J. Local Structure Analysis and Modeling of Lignin-Based Carbon Composite through the Hierarchical Decomposition of the Radial Distribution Function

The following article's content is unchanged from the above publication except for format. The publication is two-column format and below the article is in single-column format. The numbers in the section headings have also been removed. Figure and Table positions have been moved slightly to accommodate the required format.

Credit authorship contribution statement:
Dayton G. Kizzire: Investigation, software development, simulations, formal analysis, writing (original draft), data visualization, data curation. David P. Harper: Conceptualization writing – review & editing. David J. Keffer: Conceptualization, methodology, software development, supervision, formal analysis, investigation, Writing – review & editing.

## Abstract

Graphitic, amorphous, and nanostructured carbon materials are in high demand for commercial and research applications across the world. Carbonized lignin is a sustainable and domestic material that can serve as a main source of graphite and its allotropes for a myriad of applications; however due to the variability of lignin and its monomeric units, Process-Structure-Property-Performance (PSPP) relationships are often hard to define. In this work, radial distribution functions from synchrotron X-ray and neutron scattering of lignin-based carbon composites (LBCCs) are studied to characterize the local atomic environment and develop PSPP relationships. Analysis of the RDFs and development of PSPP relationships are aided by novel modelling based on the Hierarchical Decomposition of the Radial Distribution Function (HDRDF) where the RDF is modelled through a combination of static atomic structures and continuous mesoscale objects. Modelling allows iterative optimization of structural parameters and uses roughly one million times less computational resources compared to similar work with MD simulation. PSPP relationships for LBCCs defined by this work and HDRDF include increasing crystalline volume fraction, nanoscale composite density, and crystallite size with increasing reduction temperature. Further, carbon crystallite shape is found to transform from

spherical at 1050 °C, to ellipsoidal at 1500 °C, to graphitic, onion-like polyhedra and nanotube like structures at 2000 °C.

## Introduction

Innovation is flourishing in energy research where nanostructured materials play a critical role as they have enabled the development of safer, longer lasting, and higher charge density batteries, super capacitors, and fuel cells for use in electric vehicles, mobile electronics, large scale grid applications, *etc.* [95-98]. One of the primary concerns in the field of materials science is the development of process-structure-property-performance (PSPP) relationships for nanostructured materials and in general, finding optimal performance of nanostructured materials for any energy application requires the local atomic structure to be well defined. The local atomic structure is often described with the radial distribution function (RDF) or $g(r)$ where r is the separation between atoms. Neutron and x-ray scattering experiments yield the total scattering intensity function S(Q) which includes both Bragg and diffuse scattering and can be Fourier transformed to real space to represent the RDF. The RDF is an effective function for evaluating the local structure of powder, single crystal, or liquid materials containing amorphous or crystalline domains and isotropic or anisotropic orientation [22]. In battery specific research, it can also help define local order changes from cycling, nano-phase quantifications, and ion storage mechanisms [19,21,24-29,85]. When studying complex materials, interpretation of the RDF can present a significant challenge due to the nature of scattering from multiple nanoscale phases and/or amorphous phases. The process of ascribing structural features of nanomaterials to specific peaks and features of an experimentally obtained RDF is arduous for complex nanomaterials and further, the determination of an optimal structure for use in applications is quite difficult. By generating a model with experimental knowledge and simulating its RDF, researchers can directly attribute a complex nanomaterial's structural characteristics to features present in the calculated RDF [22,29,30]. To solve this critical link of PSPP relationships and obtain an accurate description of the local structure of complex materials, we must combine modelling and experimental methodologies.

Traditionally, determining the local structure of complex nanomaterials with large amorphous components is accomplished through the hypothesis of a model structure based on experimentally observed features and simulation using large-scale molecular dynamics (MD) to capture the mesoscale structure of the material. Subsequent analysis usually includes comparison of the neutron or x-ray radial distribution function (RDF) and the simulated RDF [27]. While this method is effective for testing specific composites, it produces a bottleneck when researching materials where small changes in processing have wide effects in the resultant structure and the subsequent performance of materials in

applications. Such problems would be better solved with a process where the model's structural parameters are refined iteratively; however, this is impractical with MD simulations as complex nanomaterials are generally computationally expensive due to the large system sizes required to capture the nano and meso-scale order [69]. This problem presents the need for a computational tool to quickly model and iteratively refine complex nanostructured materials without a severe computational cost.

Although there are many, some of the current endeavors in developing a generalized tool for structural analysis of complex materials include the Diffpy-Complex Modelling Framework, the TOPAS-Academic software package, DISCUS by Thomas Proffen and Reinhard Neder and RMCprofile with head developer Matt Tucker from Oak Ridge National Lab [34,36,99,100]. In 2016 Oyedele *et al.* proposed a novel, physics-based model for RDF studies known as the hierarchical decomposition of the radial distribution function method where atomistic and mesoscale models and theory are combined to construct the total RDF without arbitrary fitting parameters [31]. The first iteration of this method used six-dimensional integration and could only be employed for spherical crystallites due to the difficulty of complex integration over arbitrary geometries. The first application of this method was used to successfully model the total neutron scattering (NS) RDF of a carbon-composite as well as on a component-by-component basis against MD models carried out by McNutt *et al.* [30,31]. The MD model emulated the carbon-composites that were produced from hardwood lignin, a high-carbon byproduct of fractionated woody plants from the paper and bio-ethanol industries [13,101]. These composites were chosen for the initial tests of the hierarchical decomposition method because they have hierarchical structure, spherical crystallite domains, a significant amorphous component, and show great promise as a sustainable, domestic, and high-performance option for graphitic anodes in Li-ion batteries [13,18]. Since today's energy market is focused on providing more efficient, sustainable, and less polluting sources of energy storage, batteries constructed with bio-based and renewable materials are a necessity [102-104].

The second generation of the hierarchical decomposition method was developed in MATLAB by García-Negrón *et al*. and was implemented on a series of three hardwood-lignin-based carbon-composites (LBCCs) with increasing pyrolysis temperature. García-Negrón's model allowed iterative by-hand optimization of structural parameters such as crystallite domain size, crystalline and amorphous volume fractions, and density [37]. Modeled RDFs were compared on a component-by-component basis versus three lignin-based carbon composite MD models of 10, 50, and 90% crystallinity which emulated the carbon-composites for hardwood lignin pyrolyzed and reduced at 1050, 1500, and 2000°C

respectively [30,37]. This second implementation of the hierarchical decomposition method maintained the reduction in computational cost by six orders of magnitude compared to the computational cost in obtaining the modeled RDF via MD simulation. Further study of the lignin-based carbon-composites by García-Negrón *et al.* found that when lignin is pyrolyzed, reduced at 1050°C and processed into an anode for li-ion batteries, these lignin-based graphitic nanocomposites granted a 20% increase in specific charge capacity (444 mAh/g vs 372 mAh/g of standard graphite) as well as a high reversible capacity, low irreversible capacity loss, and high cycle life when compared to natural flake graphite and modern coated spherical particle graphitic (cSPG) anodes [18]. Additionally, García-Negrón *et al.* and McNutt *et al.* found that the carbon-composite structure varies depending on lignin feedstock and processing conditions where higher reduction temperatures deliver larger crystallite domains and a greater crystalline volume fraction [30,37].

In this work we present the third generation of the hierarchical decomposition method (dubbed HDRDF) updated to address the major needs of previous versions, including arbitrary domain geometries, preferential orientation of crystalline domains, mesoscale (a)symmetry, and automated parameter optimization. This version is developed in C++ for computational efficiency and speed, is formatted to be user-friendly by employing a text input file and is available for both single processor use and parallel computing using MPI. The aim of HDRDF is to fill a need in the scientific community for a quick and computationally efficient method of iteratively determining the local structure of complex nanomaterials.

Validation of HDRDF is carried out through comparison of modeled RDFs to a set of three experimentally obtained RDFs gathered from SNS that were used for validation for previous versions of HDRDF and can be found in the results section. HDRDF is then used to determine the crystalline and amorphous particle shapes and sizes, component volume fractions, and composite densities for a set of LBCCs synthesized by García-Negrón *et al.* at the Center for Renewable Carbon at the University of Tennessee Institute of Agriculture.

## Methods

### *Data Collection*

The data for this work was gathered at room temperature from the 11-ID-B beamline at APS with 0.2113 Å wavelength. For the hardwood, pine, and switchgrass materials, lignin was extracted from the plant matter via the organosolv process [105,106]. The kraft softwood lignin was created through the kraft process [107]. The lignin feedstocks were

carbonized according to the procedure of García-Negrón *et al.,* with reduction temperatures of 1050, 1500, and 2000 °C for each feedstock [18,21]. Samples were prepared in capillaries for the scattering experiments and triplicates of each sample were tested to account for possible sample inhomogeneity. The RDF, or *g(r),* for each sample were calculated from the x-ray scattering data with the xPDFsuite software with lower and upper limits on the Fourier transform integral of 0.1 and 22.0 $Å^{-1}$, respectively and a value of 0.8 for the polynomial smoothing function (*rpoly*) [108]. Fourier ripples are a result of the Fourier transformation from reciprocal space to real space and are considered noise in the experimental data. The Fourier ripples arise as artificial peaks in low *r* and long scale oscillations in high *r*. These ripples have been removed for $r < 3.0$ Å in our experimental data as to not introduce a significant source of error when the experimental and modeled RDFs are compared during the structural parameter optimization step of HDRDF.

***Hierarchical Decomposition of the RDF***

The hierarchical decomposition of the RDF occurs in stages with the first stage separating phases of a complex material. For a composite composed of two phases, labeled a for amorphous and c for crystalline, total RDF, $g_{tot}$, can be expressed at the first level of the decomposition as linear combination of the pair-wise components, $g_{aa}$, $g_{cc}$, and $g_{ac} = g_{ca}$, weighted by the relative atom fractions, $x_a$ and $x_c$,

$$g_{tot}(r) = x_a^2 g_{aa}(r) + 2x_a x_c g_{ac}(r) + x_c^2 g_{cc}(r) \quad (1)$$

Subsequent stages of decomposition occur to a point at which each component of the RDF can be represented with a tractable physics-based model. A detailed and rigorous explanation of the hierarchal decomposition theory is available in works by Oyedele *et al.* and García-Negrón *et al.* [31,37]. In this implementation of HDRDF, the following procedure is adopted. For RDF components representing scattering by atoms within the same phase, the second level of decomposition is into atomistic and mesoscale components,

$$g_{aa}(r) = g_{aa}^{atom}(r) + g_{aa}^{meso}(r) \quad (2.a)$$

$$g_{cc}(r) = g_{cc}^{atom}(r) + g_{cc}^{meso}(r) \quad (2.b)$$

For RDF components representing scattering by atoms within different phases, the second level of decomposition is strictly a mesoscale component,

$$g_{ac}(r) = g_{ac}^{meso}(r) \quad (2.c)$$

The practical motivation for this choice of decomposition has two origins. First, previously published molecular simulation work on lignin-based carbon composites has associated all sharp peaks with features arising from pairs of atoms contained within a single graphitic crystallite in the crystalline domain or a single graphene fragment in the amorphous domain [30]. These contributions fall within $g_{aa}$ and $g_{cc}$. Second, static models of the graphitic crystallites or graphene fragments are readily generated from existing crystal structure databases; therefore the atomic contribution is tractable. The same degree of catalogued knowledge does not extend to the interfaces, making an atomic model for $g_{ac}$ a more suitable topic for the more computationally intensive molecular simulation approach. Fortunately, for the materials, the empirical evidence supports this level of decomposition.

Specifically, the five components of the decomposition are 1) discrete atomic contribution from pairs of atoms inside a crystallite, $g_{cc}^{atom}(r)$, 2) discrete atomic contributions from pairs of atoms in the amorphous phase, $g_{aa}^{atom}(r)$, 3) mesoscale contribution between pairs of crystallites, $g_{cc}^{meso}(r)$, 4) mesoscale contribution between amorphous domains, $g_{aa}^{meso}(r)$, and 5) mesoscale contribution between crystalline and amorphous domains, $g_{ac}^{meso}(r)$. The total RDF is then calculated from a weighted sum of each component, where the weight for each component of the hierarchical decomposition of the RDF is determined by the component volume fraction and density of each phase and ensure that the total RDF converges to unity as the separation between atoms approaches infinity. Each of these contributions are detailed in Figure 3.1. In Figure 3.1, clearly sharp features arise from contributions to the RDF with atomic resolution, while broader features are associated with mesoscale components.

***Advances from Previous Implementations of HDRDF***

The primary improvement in the current version of HDRDF is the discretization of the model at the mesoscale. As shown in Figure 3.1(b), the area enclosed within the red surfaces is designated as the crystalline phase and the contiguous area outside the red surfaces the amorphous phase. In previous works, analytical solutions were derived and employed to rapidly evaluate the six-dimensional integral generating the mesoscale RDF between spherical crystallites and the four-dimensional integral generating the mesoscale RDF between parallel circular fragments of graphene. The analytical elegance was not readily amenable to arbitrary crystallite shapes or even polydispersity of spheres. In this version of HDRDF, the analytical solutions have been replaced with a fully spatially discretized model of the composite in which the multi-dimensional integrals are evaluated via hybrid Monte Carlo (MC) integration. While stochastic integration is certainly more computationally demanding compared to evaluation of analytical functions, it still requires several orders of magnitude less computational resources than the alternative, which is

molecular dynamics simulation. Moreover, numerical integration opens the door to modeling composites with arbitrary particle shape, orientation (for non-spherical particles), polydispersity and mesoscale structure (e.g. crystallites distributed on an ordered lattice versus randomly distributed crystallites).

The spatial discretization also eliminated the need of creating empirical ways to deal with experimental data that was not well modeled by spherical crystallites as was necessary in previous efforts. The analytical approach worked well for composites when the crystalline volume fraction was low and the separation between particles high. However, when the crystalline volume fraction was high, the particles began to be packed together, resulting in a flat interface between two otherwise spherical crystallites. This geometry required a sharp increase in mesoscale crystalline-crystalline component, not possible with the analytical solution. In previous versions of HDRDF, this feature in highly crystalline composites was modeled with a parameterized erfc function. This ad hoc approach is no longer necessary with the MC integration of a spatially discretized model.

As a minor note, the previous use of HDRDF to examine carbon composites contained a third level of decomposition, separating the atomic crystalline-crystalline component into contributions arising from C atoms within the same plane and C atoms in two different planes of graphite [37]. In this work, the graphitic nanocrystallite is represented as a single atomic structure. The ability to vary the d-spacing in graphite is retained by allowing the c vector of the unit cell to vary.

***Insights from Mesoscale Contributions***

Radial distribution function features that define particle shape and size are difficult to determine when viewing a total RDF but are easily constructed with the HDRDF technique. The mesoscale contributions from the hierarchal decomposition play an important role in the identification of particle shape and size and in addition can aid in the determination of mesoscale symmetry of crystalline domains in composite materials. In Figure 3.2 below, various particle shapes, sizes and symmetry are shown with their corresponding intercrystallite mesoscale contributions, $g_{cc}^{meso}(r)$, to the total RDF. The plots in Figure 3.2 show the mesoscale intercrystallite contribution to the RDF for a set of similarly sized particle shapes, a set of differently sized crystallite nanospheres, and a set of simple cubic arranged nanospheres vs randomly placed nanospheres (no symmetry). These plots are included to highlight the differences in the mesoscale contribution to the total RDF and show that the isolation and analysis of $g_{cc}^{meso}(r)$ can lead to qualitative and quantitative information when modelling sets of experimental samples. The mesoscale contributions are zero until after 3 Å since distances shorter than 3 Å are included in the discrete atomic contributions to the RDF.

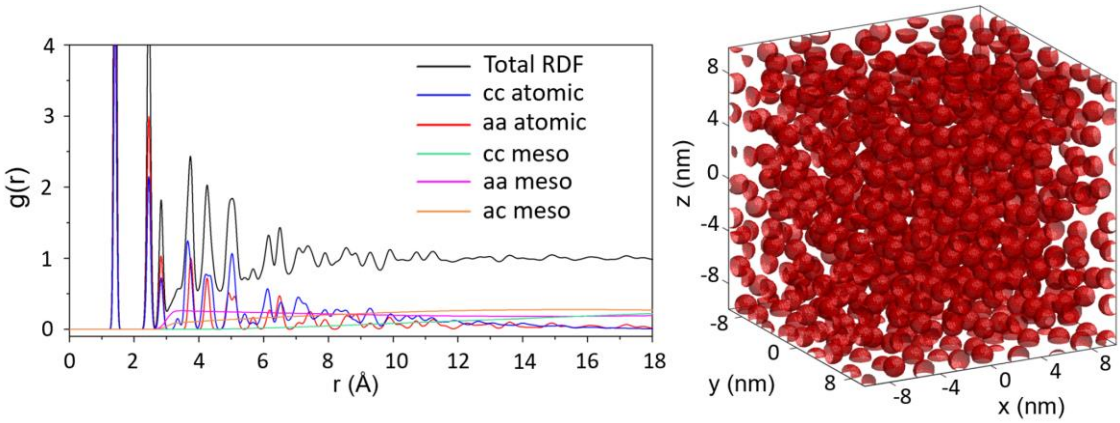


**Figure 3.1: Left –** Hierarchical decomposition of the RDF with components 1) atomic crystalline intraparticle, 2) atomic amorphous intraparticle, 3) mesoscale crystallite interparticle, 4) mesoscale amorphous interparticle, 5) mesoscale crystalline-amorphous interparticle. **Right –** Mesoscale model with 50% crystalline volume fraction and 1.5 nm diameter spherical crystallites (red) and an encapsulating amorphous matrix (white).

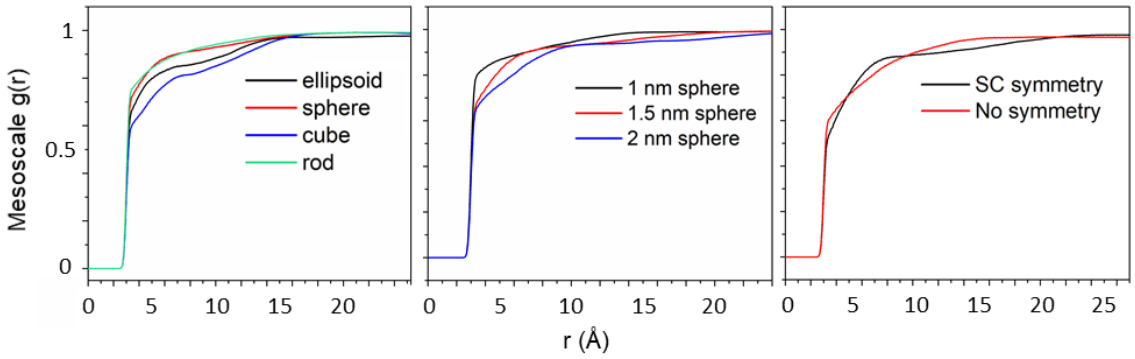


**Figure 3.2:** Intercrystallite mesoscale contributions, $g_{cc}^{meso}(r)$, to the total RDF aid in particle shape determination (left), particle size determination (center), and mesoscale particle symmetry in the composite (right).

### *Model Creation and Optimization*

In this section we describe the flow and methods of operation for the HDRDF software. Crystalline phases (three dimensional volumes cut from a bulk graphite structure) and amorphous base units (represented by graphene fragments) are input into HDRDF with their respective particle shape, lattice vectors and angles, and fractional coordinates. To handle arbitrary geometries of crystalline and amorphous domains, HDRDF allows custom cartesian coordinate inputs. These atomic models are then used to compute the atomic contributions to the RDF from the crystalline and amorphous phases by constructing a histogram of all interatomic distances and applying gaussian type anisotropic thermal noise. Next, the crystallite particles are arranged in a 3-dimensional structure according to user input (i.e. simple cubic formation, close packed, random placement, etc.) and the component-wise volume fractions. The 3-dimenstional mesoscale model is projected to a digitized 3-d mesh with 0.2 Å resolution as shown in Figure 3.1. Sections of the mesh that are not defined with crystalline particles can be defined as an encapsulating amorphous matrix. The mesoscale model is a box whose size is generated to be greater than twice the length of the experimental RDF length used for comparison. This model sizing technique avoids artifacts in the modeled RDF that could arise by using a smaller mesoscale model with periodic boundary conditions. The mesoscale components of the RDF decomposition are then constructed with Monte Carlo Integration (MCI) performed on the digitized mesh where the number of sample points for each mesoscale contribution are based on component volume fraction and component density. The mesoscale components ($g^{meso}(r)$), are then linearly interpolated to the experimental resolution (usually 0.01 Å) and the total RDF is formed from the weighted sum of the atomic and mesoscale contributions as seen in Figure 1. The total modeled RDF is then compared to experiment and a least-squares error is calculated to measure goodness of fit. Iterative optimization of structural parameters is then carried out via BFGS conjugate gradient method until the specified convergence criteria are met [109].

### *HDRDF output*

After convergence of the iterative optimization, HDRDF outputs the optimized structural parameters as well as the total modeled RDF and each component of the hierarchical decomposition. In addition, there are options to allow HDRDF to output the crystalline, amorphous, and mesoscale 3D models for visualization.

## Results and Discussion

### *Model Validation*

In order to validate HDRDF 3.0, as well as showcase the increased accuracy and functionality of this iteration of HDRDF, we apply it to carbon composites generated from hardwoods that have been analyzed by both molecular dynamics simulation as well as earlier versions of HDRDF [30,31,37]. A systematic shape, size, and crystalline volume fraction analysis was conducted for the three samples, where crystallite size and crystalline volume fraction were varied for right parallelepiped, rod, sphere, and ellipsoid particle shapes and compared for best fit to the NS RDF data. Results from this analysis agreed well with the structural parameters found in the previous version of HDRDF published by García-Negrón *et al.*, which showed the best model for this data uses spherical particles with increasing particle radius and decreasing crystalline volume fraction with the increasing carbonization temperature of the three carbon composites [37]. The RDFs for the three composites with their respective HDRDF models are shown in Figure 3.3 below with the optimized structural parameters shown in Table 1. We can see from Figure 3.3 that the magnitude of the peaks in the HDRDF model are consistent with the peak magnitudes from NS experiments. Since all peak positions are represented by HDRDF, it confirms that the graphene fragments used to model the atomic contribution for the amorphous phase are correct; if the amorphous phase contained $sp^3$ bond hybridization then peak positions in the HDRDF model would not match the NS experiments. The density for the crystalline and amorphous domains were input as 2.266 and 0.95 g/cm$^3$ respectively, consistent with literature values for crystalline graphite and both 2D and 3D amorphous graphene with $sp^2$ bonding [110]. It is important to note that the HDRDF modeled RDFs are calculated directly and thus have no short or long-range oscillations (Fourier ripples) that arise from the Fourier transform and contains no artifacts from equipment effects or sample inhomogeneity as occurs in experimentally obtained RDFs. This implies that every peak in a HDRDF modeled RDF arises due to material structure. It should also be noted that the peak widths of RDFs modeled with HDRDF are slightly narrower than the experimental comparisons due to peak broadening that occurs from ball milling of graphitic structures [111].

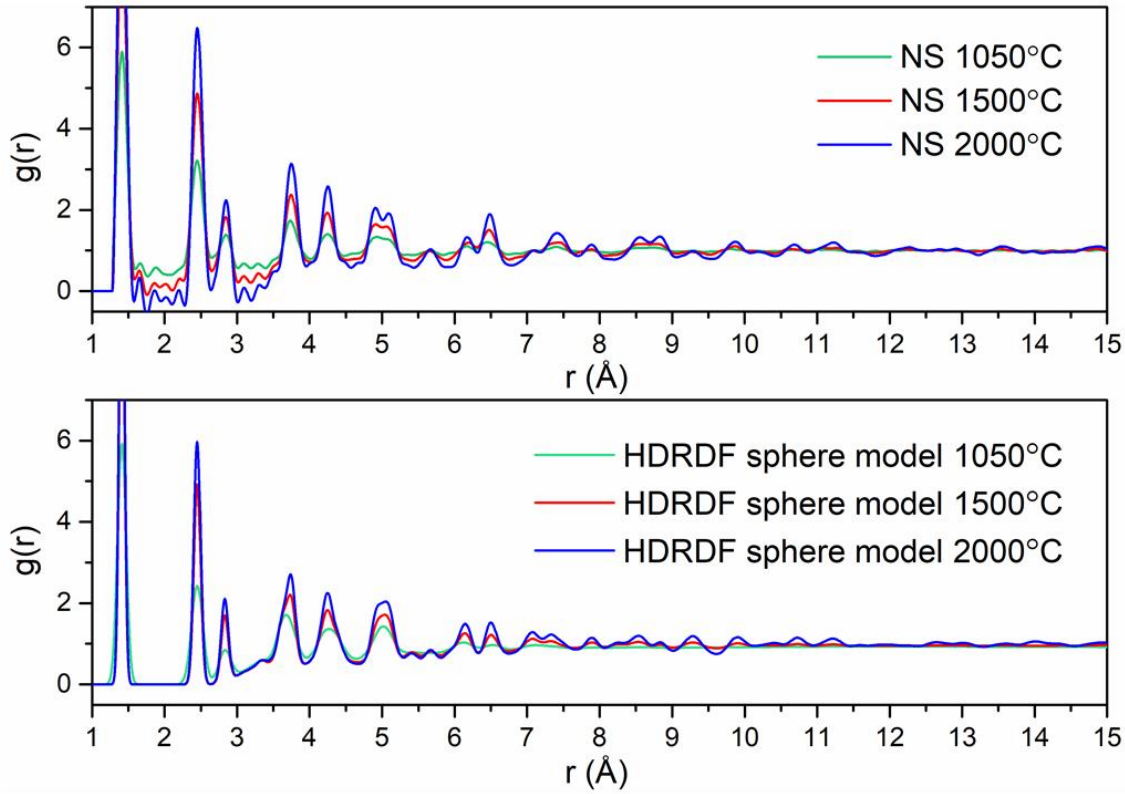


**Figure 3.3:** (Top) RDFs of lignin-based carbon composites synthesized by Tenhaeff *et al.* with increasing carbonization temperature. (Bottom) RDFs of HDRDF modeled carbon composites.

**Table 3.1:** Optimized structural parameters for lignin-based carbon composites synthesized by Tenhaeff *et al.*

| | Previous model | | | HDRDF | | |
|---|---|---|---|---|---|---|
| Pyrolysis temperature of composites (°C) | 1050 | 1500 | 2000 | 1050 | 1500 | 2000 |
| Crystallite shape | sphere | sphere | sphere | sphere | sphere | sphere |
| Crystallite radius (Å) | 5 | 7 | 17 | 5 | 7 | 17 |
| Volume fraction of crystalline domain (%) | 90 | 50 | 10 | 85 | 50 | 20 |
| Composite density (g $cm^{-3}$) | 1.94 | 1.51 | 1.38 | 2.07 | 1.61 | 1.21 |
| Graphene fragment major radius (Å) | 2.5 | 24 | 15 | 5 | 15 | 15 |
| Graphene fragment minor radius (Å) | 2.5 | 4 | 15 | 3 | 5 | 15 |
| Intraplanar thermal noise (Å) | 0.025 | 0.025 | 0.025 | 0.03 | 0.03 | 0.03 |
| Interplanar thermal noise (Å) | n/a | n/a | n/a | 0.05 | 0.05 | 0.05 |
| Composite symmetry | n/a | n/a | n/a | none | none | none |

***Modeling Carbon Composites***

It is important to note that the crystallites in the carbon composite samples synthesized by García-Negrón *et al.* [21] and tested at APS are slightly more than an order of magnitude larger than the crystallites in the carbon composite synthesized by Tenhaeff *et al.* used for HDRDF model accuracy verification. The size difference in crystallite domains can be attributed to differing lignin feedstock, synthesis methods, and post-synthesis ball milling procedure. From visual inspection of the 1050, 1500, and 2000 °C RDFs in Figure 3.4, it is evident that the local structure of the carbon composites is not only dependent upon carbonization temperature but also lignin feedstock. The woody species of lignin feedstocks including kraft softwood, pine, and hardwood share similar RDF's whereas the switchgrass samples have a comparably different structure for the 1000 and 1500 °C samples. This differing local structure can be attributed to the varying concentrations of p-hydroxyphenyl (H), guaiacyl (G), and syringyl (S) phenolic units that compose the cross-linked, amorphous structure of lignin. The carbon composites increase in crystallinity as carbonization temperature increases and the 2000 °C samples show the greatest similarity implying the structures have become more graphitic in nature. The third (2.87 Å) and fourth (3.29 Å) peaks represent the third nearest neighbor and interlayer spacing respectively as shown in the diagram in Figure 3.4. The evolution of the third peak from a shoulder to a distinct peak shows the transformation of the mostly disordered amorphous carbon composite to a more graphitic $C_6$ type structure. The stark increase in distinction of the fourth peak for 1500 and 2000 °C conveys that the carbon composite structure becomes more graphitic as planes of graphene grow and align into their equilibrium interplanar distance. Further, the increasing peak intensity past 7 Å for each increase in carbonization temperature denotes longer range order implying increased crystallinity. To reveal more about the local structure other than trends in crystallinity, we turn to modeling the carbon composites with HDRDF, with comparisons shown in Figure 3.5 and HDRDF optimized structural parameters shown in Table 3.2.

It is also important to note that there are peaks in the experimentally obtained data that do not correspond to graphite or any of its allotropes and have been confirmed through elemental analysis as varying amounts of oxygen from ether linkages that persisted through pyrolization and iron contamination from the ball milling process [21]. Since we did not include models in HDRDF for the contaminants, the modeled RDFs do not perfectly fit the experimental data. However, there is still much qualitative and quantitative information to be gleaned from the model that include shape and size for crystalline domains and the amorphous graphene fragments, component volume fractions, composite densities, and how trends in these structural parameters can aid in the understanding of the processing-

structure-property relationships. Optimized structural parameters for each model can be found in Table 3.2.

***Particle Shape and Size***

HDRDF models were made for all samples with a reduction temperature of 1050°C as well as the kraft softwood and hardwood samples reduced at 1500°C. The remaining samples with reduction temperatures of 1500 and 2000 °C possessed crystalline domains greater than 140 Å. Since these crystalline domains are much larger than the experimental RDF length of 50 Å, no meaningful crystallite shape analysis could be conducted with HDRDF and they are not modeled in this work. Experimentally, it is well established that an increase in reduction temperature leads to a corresponding increase in size of the graphitic nanocrystallites [21]. Experimental evidence regarding the relationship between nanocrystallite shape and reduction temperature is less clear. However, the TEM work of García-Negrón et al. suggests that the larger graphitic nanocrystallites that appear at high reduction temperatures are more likely to contain distinctly non-spherical geometry, presumably due to anisotropic growth of graphite in the directions parallel (100 and 010) and normal (001) to the stacked sheets. To our knowledge there is limited understanding of how choice of lignin feedstock impacts crystallite size. García-Negrón reports two nuanced observations in this regard. First, principle component analysis of RDFs suggest that differences in carbon composite local structure, resulting from variation in the distribution of lignin monomers in the source plant, tend to disappear as the reduction temperature is increased. In other words, all lignin materials will eventually form graphite if the temperature is sufficiently high. Second, differences in the size of the resulting crystallites are most obvious at the highest reduction temperatures, with kraft softwood and switchgrass yielding larger crystallites than hardwood and pine [21]. A third observation was made upon review of García-Negrón's elemental analysis of the "other" column for pyrolyzed and reduced lignin, where the "other" is strongly considered to be mostly oxygen from ether linkages and lignin monomers as well as iron contamination from ball milling [21]. Evidence for ether linkages and lignin monomers persisting post pyrolysis is present in samples reduced at 1050 °C in the experimental RDFs as there are peaks centered near 4.58 and 5.85 Å that are not present in the all-carbon HDRDF models. For the switchgrass sample specifically, the previously specified peaks are broader and there exists an additional unmodeled peak at 8.1 Å that disappears with increasing reduction temperature. The interatomic distances of an array ether linkages and lignin monomers were examined and specific atom pair distances were found that match the radial distance of the unmodeled peaks in the composites reduced at 1050 °C, including the 4.58 Å carbon-oxygen distance in the β-O-4 ether linkage. Further, these peaks decrease in intensity as reduction temperature increases which is consistent with what we expect as the ether linkages and

lignin monomers break down and oxygen is driven off by the higher reduction temperatures.

Since we know the amount of iron in the samples stays constant with increasing reduction temperature, we can attribute the change in the "other" column to the removal of oxygen. Further, comparison of x-ray diffraction peaks in all feedstocks by García-Negrón *et al.* shows that the pine and hardwood samples contained a greater amount of iron contaminants than the kraft softwood and switchgrass samples [21]. Therefore we can conclude that there is greater than 25-50% more oxygen in the kraft softwood and switchgrass samples reduced at 1050 ℃ and more than 15% less oxygen present in kraft softwood and switchgrass samples reduced at 2000 ℃ when compared to the pine and hardwood samples at the same reduction temperatures [21]. This suggests that the larger crystallites that can be seen in the kraft softwood and switchgrass HR-TEM images could be attributed to the greater amount of ether linkages present in kraft softwood and switchgrass samples post pyrolysis as they could serve as a scaffold to provide an amount of order along which crystallites could grow larger as pyrolysis temperature increases.

A systematic shape and size analysis was conducted for each of the modeled composites where sphere, ellipsoid, rod, and right parallelepiped shapes were tested and the dimensions for each shape were optimized via conjugate gradient optimization and the resulting RDFs were compared for best fit via least squares error between the experimental and modeled RDFs. Since modeled peaks at low radial distances (below 10 Å) are narrower and taller than experimental peaks due to instrumental peak broadening and inherent sample inhomogeneity/disorder not captured by HDRDF, a weighting function was applied to the least squares error calculation which emphasized the differences at longer radial distances (above 10 Å) in order to help determine particle shape and size more accurately. All samples reduced at 1050°C possessed spherical particle shapes consistent with validation data of smaller crystallites from previous neutron scattering experiments. The modeled spherical crystallites for the 1050°C samples ranged from 4.4 to 5.6 nm in diameter depending on the feedstock. As the reduction temperature increased, the HDRDF analysis confirms growth of the crystallite size and an increase in crystalline volume fraction. Furthermore, the shape of the crystallites deviates from spherical. The 1500°C samples were best fit with prolate ellipsoidal crystallites with the interplane direction acting as the major radius of 3.2 – 4.2 nm and the in-plane directions acting as minor radii of 2.4 – 3.3 nm. nm. As reduction temperature is increased the graphene planes align and equilibrate into an interplanar distance of 3.35 for kraft softwood and 3.44 nm for all other samples as can be seen by the examination of the fourth peak in the experimental RDFs in Figure 4 as well as the HDRDF fits in Figure 3.5. The adoption of surrounding amorphous planes of

graphene into crystallites contributes to the change in crystallite shape from spheres to ellipsoids. The modeled crystalline domain sizes are in good agreement with the Scherrer analysis performed on the scattering data by García-Negrón *et al.* [21]. Amorphous graphene fragments with circular and elliptical shapes were tested with the result of 2D ellipses having the better fit. The 2D ellipses possessed smaller major and minor radii than the crystallites, consistent with previous models and our physical understanding of the composite.

The HR-TEM of kraft softwood and switchgrass samples reduced at 2000 °C show primarily crystalline graphitic domains with large polygonal onion-like nanocrystallites, as well as large, elongated rod like structures that could be multi-walled carbon nanotubes or collapsed carbon nanotubes based on similarities in TEM patterns found in literature [21,83,112,113].

### *Crystalline Volume Fraction*

From visual inspection of the HR-TEM images reported by García-Negrón *et al.* [21] there is a definite increase in the crystalline volume fraction for each feedstock with increasing reduction temperature. Samples reduced at 1050 °C show a primarily amorphous structure with small amounts of nanocrystallites while samples reduced at 2000 °C show primarily graphitic and ordered structures which are most easily observed in the kraft softwood and switchgrass samples. Nanocrystallites in the pine and hardwood samples reduced at 1050 °C and 2000 °C are somewhat difficult to make out visually; however, the XRD and Scherer analysis confirm their presence with new peaks forming in the XRD pattern as reduction temperature is increased.

HDRDF models for the 1050°C samples range from 15% crystalline volume fraction for hardwood to 25% crystalline volume fraction for switchgrass. Models for the 1500°C samples found an increase in crystalline volume fractions up to 45%. These results agree well with the HR-TEM and XRD – Scherer analysis conducted by García-Negrón *et al* [21]; however, they are in disagreement with the trends modeled by McNutt *et al. [30]* who states that for the LBCCs synthesized from hardwood lignin by Tenhaeff *et al.* [13], crystalline volume fraction decreases with increasing pyrolysis temperature.

### *Composite Density*

Results from HR-TEM and x-ray diffraction analysis conducted by García-Negrón *et al.* show an increase in graphitic structure as well as a reduction in amorphous regions with increasing reduction temperature for all feedstocks [21]. This would suggest a monotonic

increase in the local composite density at the nanoscale with increasing reduction temperature; however, since the composite densities were not determined experimentally there is a degree of uncertainty. For HDRDF modeled composites the density for the crystalline and amorphous domains were input as 2.266 and 1.76 g/cm$^3$ respectively, except for the switchgrass sample reduced at 1050 °C which was better fit with an amorphous phase density of 1.69 g/cm$^3$. The amorphous carbon density was found to be greater in the models for the García-Negrón *et al.* composites when compared to the amorphous carbon density of the composites synthesized by Tenhaeff *et al.* We believe that the difference in the modeled amorphous phase density between the Tenhaeff *et al.* composites and the García-Negrón *et al.* composites can be attributed to the differences in the used feedstocks, as well as the differences in processing and carbonization of the lignin. As reduction temperature increased the modeled composite density also increased towards the density of crystalline graphite as would be expected with a larger crystalline volume fraction. The reported composite densities in Table 3.2 are likely slightly overestimated since porosity and sample packing density present in experimental samples is not captured by the model. In future updates to the HDRDF software, we plan to improve this area by including customizable options for various states of porosity in the mesoscale model.

### *HDRDF 3.0 Limitations*

As with many other modeling techniques, HDRDF 3.0 has limits on the size of a system that it can model effectively. For HDRDF the limit is dependent upon the length of the experimental RDF and the size of the crystalline domains. Since the RDF is used for local structure determination, if the average particle size is much greater than the length of the experimental RDF accurate modeling becomes difficult. When modeling nanomaterials with HDRDF 3.0, the peak heights, widths, and mesoscale features of modeled RDFs are sensitive to changes in particle size and component volume fractions; however, when crystallites have domains greater than nanoscale size, the RDFs no longer contain the information which would allow the determination of particle size or shape and the modeled RDFs resemble multiphase bulk materials instead of nanoscale composites as it is in our case for the composites reduced at 2000 °C as well as the switchgrass and pine samples reduced at 1500 °C.

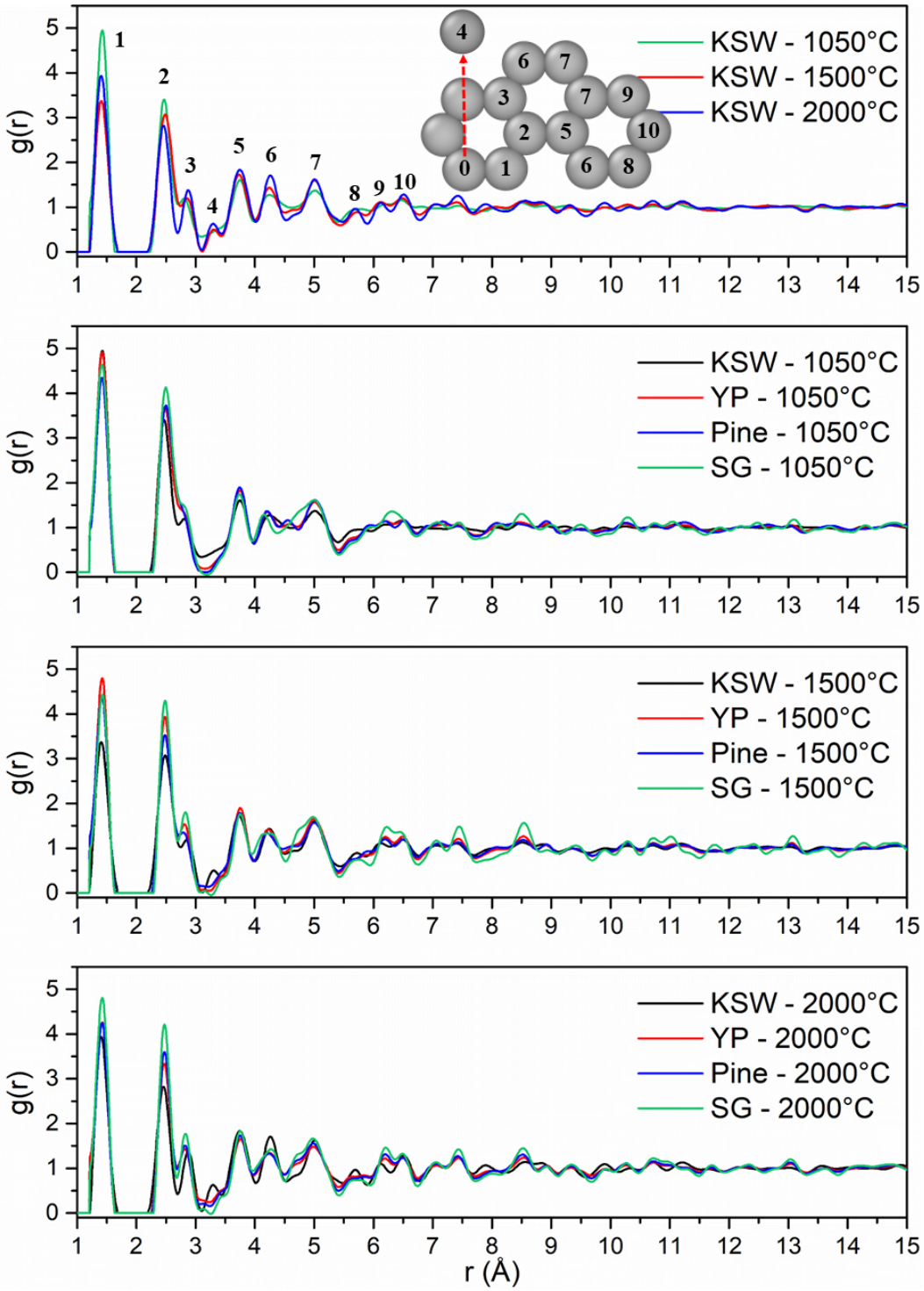


**Figure 3.4:** RDFs of lignin-based carbon composites synthesized by García-Negrón *et al*. and grouped by carbonization temperature. (Top) Diagram identifying atomic pairs and the peak to which they correspond as measured from atom 0. Atom 4 represents the interplanar spacing of graphitic planes.

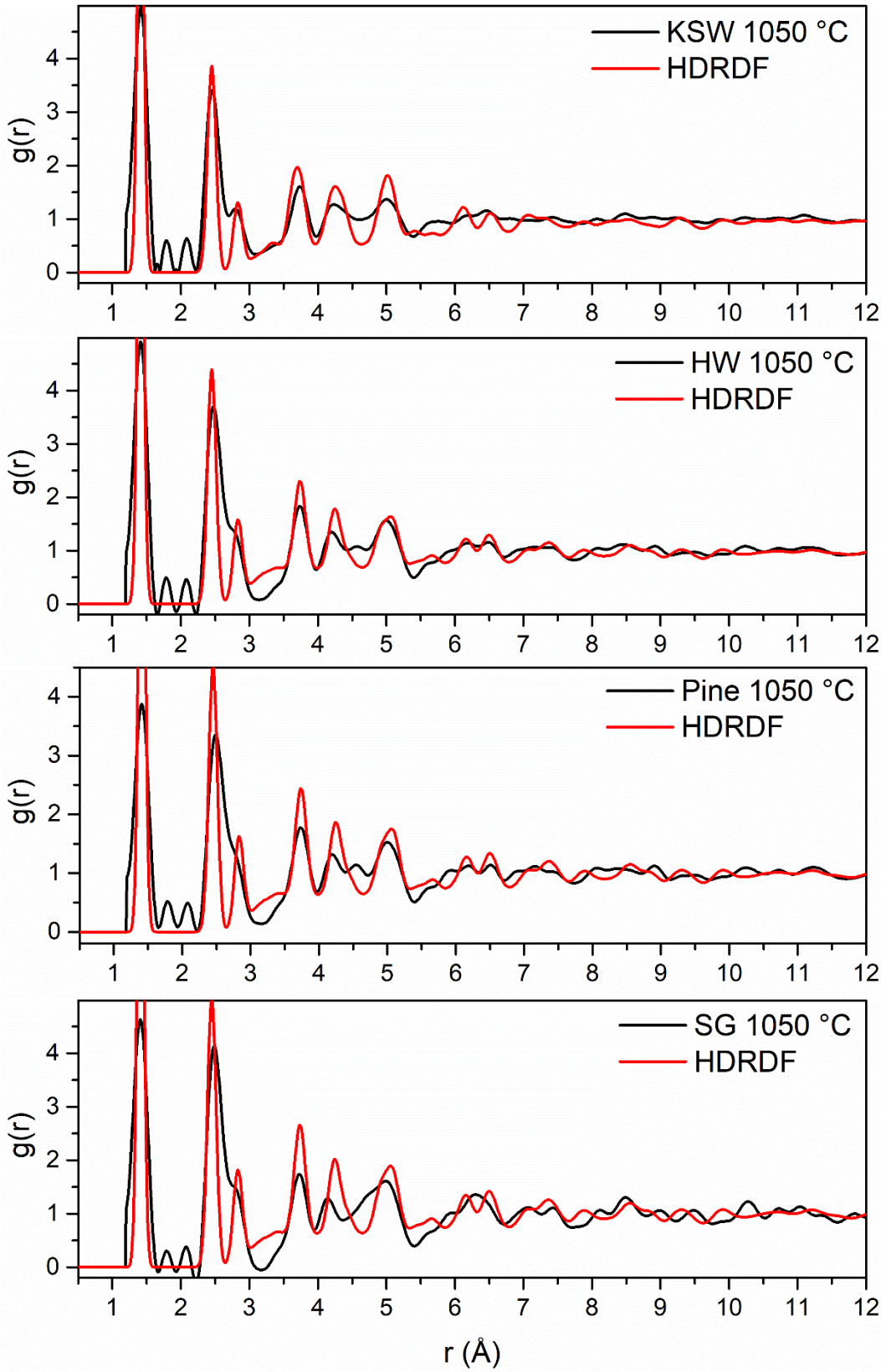


**Figure 3.5:** Synchrotron X-ray RDFs of lignin-based carbon composites reduced at 1050 °C synthesized by García-Negrón *et al.*, plotted with their respective HDRDF models.

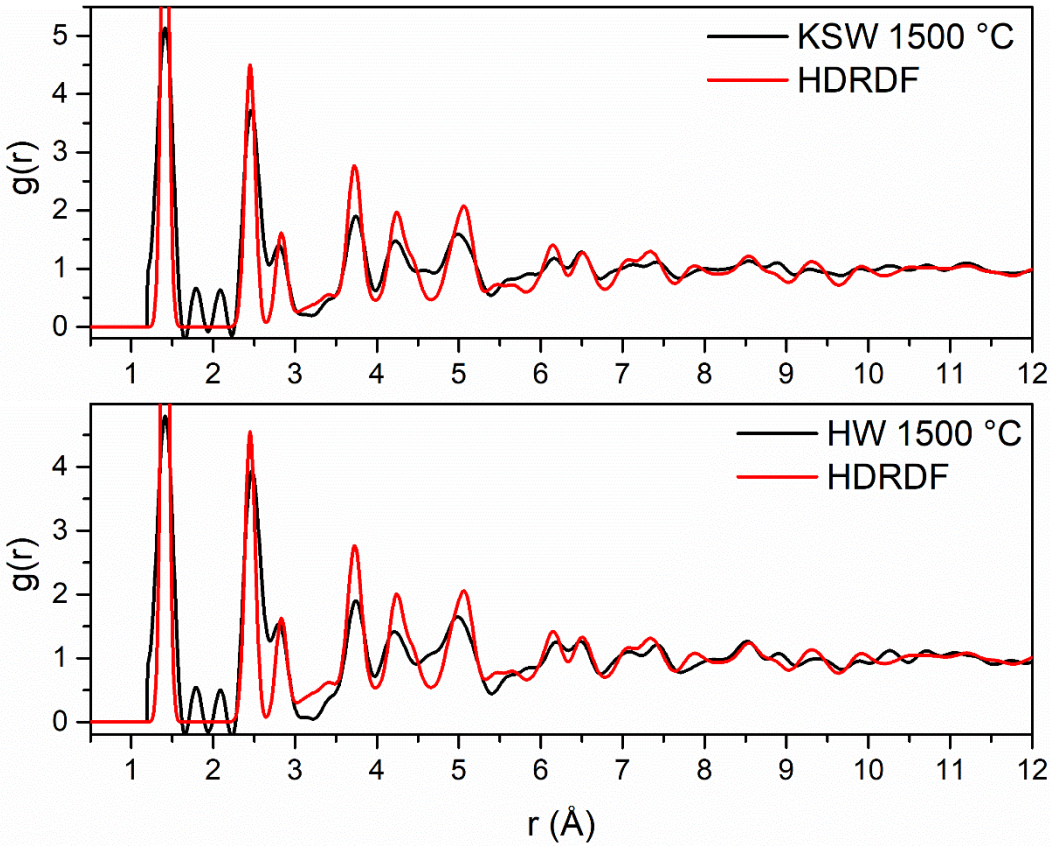


**Figure 3.5 continued:** Synchrotron X-ray RDFs of lignin-based carbon composites reduced at 1500 °C synthesized by García-Negrón *et al.*, plotted with their respective HDRDF models.

**Table 3.2:** HDRDF optimized structural and physical parameters for lignin-based carbon composites synthesized by García-Negrón *et al.*

| **Pyrolysis Temperature** | **1050°C** | | | | **1500°C** | |
|---|---|---|---|---|---|---|
| **Lignin Feedstock** | **KSW** | **HW** | **Pine** | **SG** | **KSW** | **HW** |
| Crystallite shape | sphere | sphere | sphere | sphere | ellipsoid | ellipsoid |
| Crystallite radius (Å) (x,y,z) | 22 | 23 | 24 | 28 | 28, 24, 32 | 33, 30, 42 |
| Volume fraction of crystalline domain (%) | 20 | 15 | 20 | 20 | 45 | 40 |
| Composite density (g $cm^{-3}$) | 1.943 | 1.923 | 1.941 | 1.810 | 2.041 | 2.022 |
| Graphene fragment major radius (Å) | 10 | 12 | 14 | 16 | 18 | 21 |
| Graphene fragment minor radius (Å) | 8 | 8 | 11 | 12 | 14 | 13 |
| Intraplanar thermal noise (Å) | 0.04 | 0.04 | 0.04 | 0.04 | 0.04 | 0.04 |
| Interplanar thermal noise (Å) | 0.06 | 0.06 | 0.06 | 0.06 | 0.06 | 0.06 |

## IV. Conclusions

The neutron and x-ray scattering data of the lignin-based carbon composites (LBCCs) generated by Tenhaeff *et al.* and García-Negrón *et al.* respectively were successfully modeled using HDRDF and granted both quantitative and qualitative understandings of the complex material structure in addition to the identification of nanoparticle shape. With the aid of HDRDF, trends in PSPP relationships were identified as increasing crystallite size, crystalline volume fraction, and composite density as well as the transformation from spherical crystalline particles to ellipsoids as reduction temperature was increased and the composites became more graphitic in nature. Through modeling with HDRDF it was found that the amorphous carbon phase of switchgrass reduced at 1050 °C is less dense compared to other feedstocks and for all feedstocks the nanoscale composite density of LBCCs increases with increasing reduction temperature. The average interplanar distance in crystallites was found to be 3.44 nm for all feedstocks at all reduction temperatures except for kraft softwood which had an interplanar distance of 3.35 nm, like that of AB stacked graphite. Through a combination of modeling with HDRDF and visual analysis of HR-TEM images, the crystalline volume fraction was determined to increase with increasing reduction temperature for all feedstocks which become partially graphitic at a reduction temperature of 2000 °C. The crystalline volume fraction varied between 15-20% for feedstocks reduced at 1050 °C and 40-45% for feedstocks reduced at 1500 °C. The transition from spherical to ellipsoidal particle shapes as reduction temperature was increased from 1050 to 1500 °C was attributed to the adoption of amorphous graphene particles into the crystalline nanoparticles. It is also suggested that the higher oxygen content found in the kraft softwood and switchgrass samples is due to higher amounts of ether linkages and lignin monomers that persisted through pyrolysis and acted as a scaffold, providing structure for crystallites to grow into graphitic structures more rapidly. Further, additional inspection of the HR-TEM of kraft softwood and switchgrass reduced at 2000 °C suggests that the large rod-like crystallites could be multiwalled carbon nanotubes.

The HDRDF software can now be used on parallel architectures and allows models with arbitrary domain geometries. Structural parameters are optimized via conjugate gradient optimization and crystalline/amorphous domain shapes can be identified via least-error analysis, greatly reducing the human time, effort, and error of hand-eye fitting that was present in previous models. HDRDF was able to achieve a reduction in computational cost of five orders of magnitude compared to molecular dynamics simulations of these LBCCs. HDRDF 3.0 can now be considered a generalized physics-based tractable model for rapid modeling and understanding of the local structure of complex composite materials with only a small computational cost. Plans for future updates involve modules for including crystalline and amorphous polydispersity, customizable states of porosity in the mesoscale model as well as multiple crystalline and amorphous phases.

## V. References


1. Xie J, Lu YC. A retrospective on lithium-ion batteries. Nat Commun. 2020 May 19;11(1):2499.
2. Chikkannanavar SB, Bernardi DM, Liu L. A review of blended cathode materials for use in Li-ion batteries. Journal of Power Sources. 2014;248:91-100.
3. Daniel C, Mohanty D, Li J, et al. Cathode materials review. 2014. p. 26-43.
4. Desilvestro J, Haas O. Metal Oxide Cathode Materials for Electrochemical Energy Storage: A Review. J Electrochem Soc. 2019;137(1):5C-22C.
5. Kucinskis G, Bajars G, Kleperis J. Graphene in lithium ion battery cathode materials: A review. Journal of Power Sources. 2013;240:66-79.
6. Ma Z, Yuan X, Li L, et al. A review of cathode materials and structures for rechargeable lithium–air batteries. Energy & Environmental Science. 2015;8(8):2144-2198.
7. Manthiram A. A reflection on lithium-ion battery cathode chemistry. Nat Commun. 2020 Mar 25;11(1):1550.
8. Sun C, Hui R, Roller J. Cathode materials for solid oxide fuel cells: a review. Journal of Solid State Electrochemistry. 2009;14(7):1125-1144.
9. Olson DW, Virta RL, Mahdavi M, et al. Natural graphite demand and supply—Implications for electric vehicle battery requirements. Geoscience for the Public Good and Global Development: Toward a Sustainable Future. Geological Society of America Special Papers2016. p. 67-77.
10. Guoping W, Bolan Z, Min Y, et al. A modified graphite anode with high initial efficiency and excellent cycle life expectation. Solid State Ion. 2005;176(9-10):905-909.
11. Yoshio M, Wang H, Fukuda K. Spherical carbon-coated natural graphite as a lithium-ion battery-anode material. Angew Chem Int Ed Engl. 2003 Sep 15;42(35):4203-6.
12. Yoshio M, Wang H, Fukuda K, et al. Improvement of natural graphite as a lithium-ion battery anode material, from raw flake to carbon-coated sphereElectronic supplementary information (ESI) available: colour versions of Figs. 6, 8 and 9. See http://www.rsc.org/suppdata/jm/b3/b316702j. Journal of Materials Chemistry. 2004;14(11).
13. Tenhaeff WE, Rios O, More K, et al. Highly Robust Lithium Ion Battery Anodes from Lignin: An Abundant, Renewable, and Low-Cost Material. Advanced Functional Materials. 2014 Jan;24(1):86-94.
14. Bajwa DS, Pourhashem G, Ullah AH, et al. A concise review of current lignin production, applications, products and their environmental impact. Industrial Crops and Products. 2019;139.
15. Rowell RM. Handbook of wood chemistry and wood composition. CRC Press; 2012.
16. Luo H, Abu-Omar MM. Chemicals From Lignin. Encyclopedia of Sustainable Technologies2017. p. 573-585.

17. Ragauskas AJ, Beckham GT, Biddy MJ, et al. Lignin valorization: improving lignin processing in the biorefinery. Science. 2014 May 16;344(6185):1246843.
18. García-Negrón V, Phillip ND, Li J, et al. Processing-Structure-Property Relationships for Lignin-Based Carbonaceous Materials Used in Energy-Storage Applications. Energy Technology. 2017;5(8):1311-1321.
19. McNutt NW, McDonnell M, Rios O, et al. Li-Ion Localization and Energetics as a Function of Anode Structure. ACS Appl Mater Interfaces. 2017 Mar 1;9(8):6988-7002.
20. McNutt NW, Rios O, Maroulas V, et al. Interfacial Li-ion localization in hierarchical carbon anodes. Carbon. 2017;111:828-834.
21. García-Negrón V, Kizzire DG, Rios O, et al. Elucidating nano and meso-structures of lignin carbon composites: A comprehensive study of feedstock and temperature dependence. Carbon. 2020;161:856-869.
22. Takeshi Egami SJLB. Underneath the Bragg Peaks: Structural Analysis of Complex Materials. Elsevier; 2003. (Cahn RW, editor. Pergamon Materials Series).
23. Narten AH, Vaslow F, Levy HA. Diffraction pattern and structure of aqueous lithium chloride solutions. The Journal of Chemical Physics. 1973;58(11):5017-5023.
24. Lin R, Hu E, Liu M, et al. Anomalous metal segregation in lithium-rich material provides design rules for stable cathode in lithium-ion battery. Nat Commun. 2019 Apr 9;10(1):1650.
25. Ohara K, Mitsui A, Mori M, et al. Structural and electronic features of binary Li(2)S-P(2)S(5) glasses. Sci Rep. 2016 Feb 19;6:21302.
26. Wang X, Tan S, Yang X-Q, et al. Pair distribution function analysis: Fundamentals and application to battery materials. Chinese Physics B. 2020;29(2).
27. Dhungana KB, Faria LF, Wu B, et al. Structure of cyano-anion ionic liquids: X-ray scattering and simulations. J Chem Phys. 2016 Jul 14;145(2):024503.
28. Zhao E, Zhang M, Wang X, et al. Local structure adaptability through multi cations for oxygen redox accommodation in Li-Rich layered oxides. Energy Storage Materials. 2020;24:384-393.
29. Shan X, Guo F, Page K, et al. Framework Doping of Ni Enhances Pseudocapacitive Na-Ion Storage of (Ni)MnO2 Layered Birnessite. Chemistry of Materials. 2019;31(21):8774-8786.
30. McNutt NW, Rios O, Feygenson M, et al. Structural analysis of lignin-derived carbon composite anodes. Journal of Applied Crystallography. 2014;47(5):1577-1584.
31. Oyedele A, McNutt NW, Rios O, et al. Hierarchical Model for the Analysis of Scattering Data of Complex Materials. Jom. 2016;68(6):1583-1588.
32. Krayzman V, Levin I. Reverse Monte Carlo refinements of nanoscale atomic correlations using powder and single-crystal diffraction data. Journal of Applied Crystallography. 2012;45(1):106-112.
33. Tucker MG, Keen DA, Dove MT, et al. RMCProfile: reverse Monte Carlo for polycrystalline materials. J Phys Condens Matter. 2007 Aug 22;19(33):335218.

34. Tucker MGD, M.T.; Keen, D.A. Application of the reverse Monte Carlo method to crystalline materials. Journal of Applied Crystallography. 2001;34:630-638.
35. Page K, Hood TC, Proffen T, et al. Building and refining complete nanoparticle structures with total scattering data. Journal of Applied Crystallography. 2011;44(2):327-336.
36. Proffen TEN, R.B. DISCUS: a program for diffuse scattering and defect-structure simulation. Journal of Applied Crystallography. 1997;30:171-175.
37. García-Negrón V, Oyedele AD, Ponce E, et al. Evaluation of nano- and mesoscale structural features in composite materials through hierarchical decomposition of the radial distribution function. Journal of Applied Crystallography. 2018;51(1):76-86.
38. Ogata S, Ohba N, Kouno T. Multi-Thousand-Atom DFT Simulation of Li-Ion Transfer through the Boundary between the Solid–Electrolyte Interface and Liquid Electrolyte in a Li-Ion Battery. The Journal of Physical Chemistry C. 2013;117(35):17960-17968.
39. Dobrota AS, Pašti IA, Mentus SV, et al. Functionalized graphene for sodium battery applications: the DFT insights. Electrochimica Acta. 2017;250:185-195.
40. Jonsson E, Johansson P. Modern battery electrolytes: ion-ion interactions in Li+/Na+ conductors from DFT calculations. Phys Chem Chem Phys. 2012 Aug 14;14(30):10774-9.
41. Xu Z, Lv X, Chen J, et al. DFT investigation of capacious, ultrafast and highly conductive hexagonal Cr2C and V2C monolayers as anode materials for high-performance lithium-ion batteries. Phys Chem Chem Phys. 2017 Mar 15;19(11):7807-7819.
42. Yahia M, Vergnet J, Saubanere M, et al. Unified picture of anionic redox in Li/Na-ion batteries. Nat Mater. 2019 May;18(5):496-502.
43. Senftle TP, Hong S, Islam MM, et al. The ReaxFF reactive force-field: development, applications and future directions. npj Computational Materials. 2016;2(1).
44. Papanek PR, M.; Fischer, J.E. Lithium Insertion in Disordered Carbon-Hydrogen Alloys: Intercalation vs Colvalent Binding. Chemistry of Materials. 1996;8(7):1519-1526.
45. Liang Y, Lai WH, Miao Z, et al. Nanocomposite Materials for the Sodium-Ion Battery: A Review. Small. 2018 Feb;14(5).
46. Islam MS, Fisher CA. Lithium and sodium battery cathode materials: computational insights into voltage, diffusion and nanostructural properties. Chem Soc Rev. 2014 Jan 7;43(1):185-204.
47. Chayambuka K, Mulder G, Danilov DL, et al. Sodium-Ion Battery Materials and Electrochemical Properties Reviewed. Advanced Energy Materials. 2018;8(16).
48. Barpanda P, Oyama G, Nishimura S, et al. A 3.8-V earth-abundant sodium battery electrode. Nat Commun. 2014 Jul 17;5:4358.
49. Ganesh P, Kim J, Park C, et al. Binding and Diffusion of Lithium in Graphite: Quantum Monte Carlo Benchmarks and Validation of van der Waals Density Functional Methods. J Chem Theory Comput. 2014 Dec 9;10(12):5318-23.

50. Meng YS, Arroyo-de Dompablo ME. First principles computational materials design for energy storage materials in lithium ion batteries [10.1039/B901825E]. Energy & Environmental Science. 2009;2(6):589-609.
51. Raju M, Ganesh P, Kent PR, et al. Reactive Force Field Study of Li/C Systems for Electrical Energy Storage. J Chem Theory Comput. 2015 May 12;11(5):2156-66.
52. van Duin ACT, Dasgupta S, Lorant F, et al. ReaxFF: A reactive force field for hydrocarbons. Journal of Physical Chemistry A. 2001 Oct;105(41):9396-9409.
53. Li Y, Lu Y, Adelhelm P, et al. Intercalation chemistry of graphite: alkali metal ions and beyond. Chem Soc Rev. 2019 Aug 27;48(17):4655-4687.
54. Okamoto Y. Density Functional Theory Calculations of Alkali Metal (Li, Na, and K) Graphite Intercalation Compounds. The Journal of Physical Chemistry C. 2014 2014/01/09;118(1):16-19.
55. Wan W, Wang H. Study on the First-Principles Calculations of Graphite Intercalated by Alkali Metal (Li, Na, K). Int J Electrochem Sci. 2015 04/01;10:3177-3184.
56. Dahbi M, Yabuuchi N, Kubota K, et al. Negative electrodes for Na-ion batteries. Physical Chemistry Chemical Physics. 2014;16(29):15007-15028.
57. Yabuuchi N, Kubota K, Dahbi M, et al. Research Development on Sodium-Ion Batteries. Chemical Reviews. 2014 Dec;114(23):11636-11682.
58. Hossain S, Saleh Y, Loutfy R. Carbon-carbon composite as anodes for lithium-ion battery systems. Journal of Power Sources. 2001 Jun;96(1):5-13.
59. Daniel C. Materials and processing for lithium-ion batteries [Article]. Jom. 2008 Sep;60(9):43-48.
60. Liu P, Wu HQ. Diffusion of lithium in carbon [Article]. Solid State Ion. 1996 Nov;92(1-2):91-97.
61. Winter M, Novak P, Monnier A. Graphites for lithium-ion cells: The correlation of the first-cycle charge loss with the Brunauer-Emmett-Teller surface area [Article]. J Electrochem Soc. 1998 Feb;145(2):428-436.
62. Chatterjee S, Clingenpeel A, McKenna A, et al. Synthesis and characterization of lignin-based carbon materials with tunable microstructure. Rsc Advances. 2014;4(9):4743-4753.
63. Hasegawa M, Nishidate K, Iyetomi H. Energetics of interlayer binding in graphite: The semiempirical approach revisited. Physical Review B. 2007 Sep;76(11).
64. Lebedeva IV, Knizhnik AA, Popov AM, et al. Interlayer interaction and relative vibrations of bilayer graphene. Physical Chemistry Chemical Physics. 2011;13(13):5687-5695.
65. Rai A, Warrier M, Schneider R. A hierarchical multi-scale method to simulate reactive-diffusive transport in porous media. Computational Materials Science. 2009 Aug;46(2):469-478.
66. Tsai JL, Tu JF. Characterizing mechanical properties of graphite using molecular dynamics simulation. Materials & Design. 2010 Jan;31(1):194-199.
67. Dou XW, Hasa I, Saurel D, et al. Hard carbons for sodium-ion batteries: Structure, analysis, sustainability, and electrochemistry. Materials Today. 2019 Mar;23:87-104.

68. Hjertenaes E, Nguyen AQ, Koch H. A ReaxFF force field for sodium intrusion in graphitic cathodes. Phys Chem Chem Phys. 2016 Nov 23;18(46):31431-31440.
69. McNutt NW, Wang Q, Rios O, et al. Entropy-driven structure and dynamics in carbon nanocrystallites. Journal of Nanoparticle Research. 2014;16(4).
70. Kim H, Hong J, Yoon G, et al. Sodium intercalation chemistry in graphite. Energy & Environmental Science. 2015;8(10):2963-2969.
71. Barrera GD, Colognesi D, Mitchell PCH, et al. LDA or GGA? A combined experimental inelastic neutron scattering and ab initio lattice dynamics study of alkali metal hydrides. Chemical Physics. 2005 Oct;317(2-3):119-129.
72. Berliner R, Fajen O, Smith HG, et al. NEUTRON POWDER-DIFFRACTION STUDIES OF LITHIUM, SODIUM, AND POTASSIUM METAL. Physical Review B. 1989 Dec;40(18):12086-12097.
73. Delmas C. Sodium and Sodium-Ion Batteries: 50 Years of Research. Advanced Energy Materials. 2018;8(17):1703137.
74. Adamson A, Väli R, Paalo M, et al. Peat-derived hard carbon electrodes with superior capacity for sodium-ion batteries. RSC Advances. 2020;10(34):20145-20154.
75. Kubota K, Shimadzu S, Yabuuchi N, et al. Structural Analysis of Sucrose-Derived Hard Carbon and Correlation with the Electrochemical Properties for Lithium, Sodium, and Potassium Insertion. Chemistry of Materials. 2020;32(7):2961-2977.
76. Moriwake H, Kuwabara A, Fisher CAJ, et al. Why is sodium-intercalated graphite unstable? [10.1039/C7RA06777A]. RSC Advances. 2017;7(58):36550-36554.
77. Olsson E, Cottom J, Au H, et al. Elucidating the Effect of Planar Graphitic Layers and Cylindrical Pores on the Storage and Diffusion of Li, Na, and K in Carbon Materials. Advanced Functional Materials. 2020;30(17).
78. Rao X, Lou Y, Chen J, et al. Polyacrylonitrile Hard Carbon as Anode of High Rate Capability for Lithium Ion Batteries [Original Research]. Frontiers in Energy Research. 2020 2020-January-28;8(3).
79. Wang K, Jin Y, Sun S, et al. Low-Cost and High-Performance Hard Carbon Anode Materials for Sodium-Ion Batteries. ACS Omega. 2017 Apr 30;2(4):1687-1695.
80. Yu L, Hsieh C-T, Keffer DJ, et al. Hierarchical Lignin-Based Carbon Matrix and Carbon Dot Composite Electrodes for High-Performance Supercapacitors. ACS Omega. 2021 2021/03/23;6(11):7851-7861.
81. Lu Y, Lu Y-C, Hu H-Q, et al. Structural Characterization of Lignin and Its Degradation Products with Spectroscopic Methods. Journal of Spectroscopy. 2017;2017:1-15.
82. Hosseinaei O, Harper DP, Bozell JJ, et al. Role of Physicochemical Structure of Organosolv Hardwood and Herbaceous Lignins on Carbon Fiber Performance. ACS Sustainable Chemistry & Engineering. 2016;4(10):5785-5798.
83. Gindl-Altmutter W, Köhnke J, Unterweger C, et al. Lignin-based multiwall carbon nanotubes. Composites Part A: Applied Science and Manufacturing. 2019;121:175-179.
84. Xiao B, Rojo T, Li X. Hard Carbon as Sodium-Ion Battery Anodes: Progress and Challenges. ChemSusChem. 2019 Jan 10;12(1):133-144.

85. Kizzire DG, Richter AM, Harper DP, et al. Lithium and sodium ion binding in nanostructured carbon composites. Molecular Simulation. 2020:1-10.
86. Han Y, Jiang D, Zhang J, et al. Development, applications and challenges of ReaxFF reactive force field in molecular simulations. Frontiers of Chemical Science and Engineering. 2015;10(1):16-38.
87. Calvo-Munoz EM, Selvan ME, Xiong R, et al. Applications of a general random-walk theory for confined diffusion. Phys Rev E Stat Nonlin Soft Matter Phys. 2011 Jan;83(1 Pt 1):011120.
88. Plimpton S. FAST PARALLEL ALGORITHMS FOR SHORT-RANGE MOLECULAR-DYNAMICS. Journal of Computational Physics. 1995 Mar;117(1):1-19.
89. Stratford JM, Allan PK, Pecher O, et al. Mechanistic insights into sodium storage in hard carbon anodes using local structure probes. Chem Commun (Camb). 2016 Oct 13;52(84):12430-12433.
90. Au H, Alptekin H, Jensen ACS, et al. A revised mechanistic model for sodium insertion in hard carbons. Energy & Environmental Science. 2020;13(10):3469-3479.
91. Winter M, Besenhard JO, Spahr ME, et al. Insertion Electrode Materials for Rechargeable Lithium Batteries. Advanced Materials. 1998;10(10).
92. Zhang N, Tang H. Dissecting anode swelling in commercial lithium-ion batteries. Journal of Power Sources. 2012;218:52-55.
93. Persson K, Sethuraman VA, Hardwick LJ, et al. Lithium Diffusion in Graphitic Carbon. The Journal of Physical Chemistry Letters. 2010;1(8):1176-1180.
94. Koh YW, Manzhos S. Curvature drastically changes diffusion properties of Li and Na on graphene. MRS Communications. 2013;3(3):171-175.
95. Chen XB, Li C, Gratzel M, et al. Nanomaterials for renewable energy production and storage. Chemical Society Reviews. 2012;41(23):7909-7937.
96. Zhang QF, Uchaker E, Candelaria SL, et al. Nanomaterials for energy conversion and storage [Review]. Chemical Society Reviews. 2013;42(7):3127-3171.
97. Dai LM, Chang DW, Baek JB, et al. Carbon Nanomaterials for Advanced Energy Conversion and Storage [Review]. Small. 2012 Apr;8(8):1130-1166.
98. Yan Y, Chen G, She P, et al. Mesoporous Nanoarchitectures for Electrochemical Energy Conversion and Storage. Adv Mater. 2020 Nov;32(44):e2004654.
99. Juhas P, Farrow CL, Yang XH, et al. Complex modeling: a strategy and software program for combining multiple information sources to solve ill posed structure and nanostructure inverse problems. Acta Crystallographica a-Foundation and Advances. 2015 Nov;71:562-568.
100. Coelho AA. TOPAS and TOPAS-Academic: an optimization program integrating computer algebra and crystallographic objects written in C plus. Journal of Applied Crystallography. 2018 Feb;51:210-218.
101. Saito T, Brown RH, Hunt MA, et al. Turning renewable resources into value-added polymer: development of lignin-based thermoplastic. Green Chemistry. 2012;14(12):3295-3303.

102. Huang Y, Kormakov S, He X, et al. Conductive Polymer Composites from Renewable Resources: An Overview of Preparation, Properties, and Applications. Polymers (Basel). 2019 Jan 22;11(2).
103. Baroncini EA, Stanzione JF, 3rd. Incorporating allylated lignin-derivatives in thiol-ene gel-polymer electrolytes. Int J Biol Macromol. 2018 Jul 1;113:1041-1051.
104. Stanzione J, La Scala J. Sustainable polymers and polymer science: Dedicated to the life and work of Richard P. Wool. Journal of Applied Polymer Science. 2016;133(45).
105. Bozell JJ, Black SK, Myers M, et al. Solvent fractionation of renewable woody feedstocks: Organosolv generation of biorefinery process streams for the production of biobased chemicals. Biomass & Bioenergy. 2011 Oct;35(10):4197-4208.
106. J. Bozell, D. Harper, N. Labbe, et al., inventors; University of Tennessee Research

Foundation, assignee. Comprehensive Process for Selectively Separating Lignocellulosic Biomass into Purified Components with High Yield. United States patent US 10,145,063. 2017.
107. Tran H. The Kraft Chemical Recovery Process. 2008.
108. Yang X, Juhas P, Farrow CL, et al. xPDFsuite: an end-to-end software solution for high throughput pair distribution function transformation, visualization and analysis. Journal of Applied Crystallography. 2015.
109. Byrd RH, Lu PH, Nocedal J, et al. A LIMITED MEMORY ALGORITHM FOR BOUND CONSTRAINED OPTIMIZATION. Siam Journal on Scientific Computing. 1995 Sep;16(5):1190-1208.
110. Bhattarai B, Biswas P, Atta-Fynn R, et al. Amorphous graphene: a constituent part of low density amorphous carbon. Phys Chem Chem Phys. 2018 Jul 25;20(29):19546-19551.
111. Petkov V, Ren Y, Kabekkodu S, et al. Atomic pair distribution functions analysis of disordered low-Z materials. Phys Chem Chem Phys. 2013 Jun 14;15(22):8544-54.
112. Jurkiewicz K, Pawlyta M, Zygadło D, et al. Evolution of glassy carbon under heat treatment: correlation structure–mechanical properties. Journal of Materials Science. 2017;53(5):3509-3523.
113. Trayner S, Hao A, Downes R, et al. High-resolution TEM analysis of flatten carbon nanotube packing in nanocomposites. Synthetic Metals. 2015;204:103-109.

# CONCLUSION

## Per Chapter Conclusions

### *I. Lithium and Sodium Ion Binding in Nanostructured Carbon Composites*

Reactive molecular dynamics simulations were performed for a single carbon nanocrystallite embedded in an amorphous graphene fragment matrix with lithium and sodium ion loading conditions. Reactive simulations were also performed for lithium and sodium metals and hydrides. Results from the simulations of the lithiated single crystallite reveal that the most preferential binding location for lithium is at the hydrogen dense interface between the nanocrystalline domain and the amorphous domain. The simulations of the lithium metal and hydrides revealed that lithium attempt to form a lithium hydride like structure but are prevented since the lithium are strongly tethered to the relatively immobile carbon structure. Lithium can be reversibly stored at a higher density this way compared to intercalation within graphite. The reactive simulations of the sodiated carbon system showed that the most energetically favorable position for sodium is in the intercalation sites, although this state wouldn't be available in high charge density applications since the barrier to graphic intercalation is high for sodium. The sodium metal and hydride simulations revealed that sodium will not preferentially bind to hydrogen, but instead prefer to localize in the amorphous carbon domain and thus has a fundamentally different storage mechanism than lithium in these carbon composite environments. Larger simulations were needed to define the sodium ion storage mechanism.

### *II. Lithium and Sodium Ion Binding Mechanisms and Diffusion Rates in Lignin-Based Hard Carbon Models*

In this work, reactive molecular dynamics simulations were performed on three lignin based hard carbon models with 10, 50, and 90% crystalline volume fraction with lithium and sodium initialized in either the amorphous graphene domain or intercalated between layers of carbon nanocrystallites. The volume change between empty and lithiated/sodiated systems was calculated to determine swelling percentage. Lithiated and sodiated systems with an average charge density of ~120 mAh/g averaged 9% and 14% swelling, respectively. Consistent with previous work, lithium migrated to the hydrogen dense interfacial domain regardless of initial domain. Examination of system snapshots in coordination with charge and energy distributions shows that sodium will preferentially adsorb to the surface of graphene fragments and basal faces of nanocrystallites, while a small fraction of the sodium will bind at intercalation sites at the edges of nanocrystallites

where the graphitic planes have shifted and formed a wider d-spacing; however, we do not observe sodium migrating to deeper intercalation positions within the nanocrystallites. In systems with moderate porosity and low crystalline volume fraction we find that sodium will aggregate and bind to each other along graphene sheets that define the boundaries of porous regions of the hard carbon models. From these reactive simulations, the adsorption, edge-intercalation and pore filling sodiation scheme is supported for lignin based hard carbon anodes and suggests that lignin based hard carbons can be a viable anode material for high charge density Na-ion batteries.

The mean square displacement was calculated from the unwrapped coordinates of ions in the MD simulations and extended using confined random walk theory to the infinite-time limit as required by the Einstein relation for calculation of the self-diffusion coefficients. It was found that systems with larger, curved sheets of graphene, low crystalline volume fraction, and moderate porosity offer the highest diffusion rates for sodium ions at ~$10^{-7}$ $cm^2/s$, on par with that of lithium in pristine graphite. Accumulated results from these simulations suggest that a lignin based hard carbon anode featuring high charge capacity and a high ion diffusion rate for Na-ion batteries would be optimized by obtaining low crystalline volume fraction, a large fraction of curved graphene fragments, and moderate porosity. For high charge density in Li-ion batteries with lignin based hard carbon anodes, it is suggested that the LBCC have small nanocrystallites and graphene fragments to maximize the hydrogen dense interfacial regions where lithium can bind at the highest density.

### *III. Local Structure Analysis and Modeling of Lignin-Based Carbon Composite through the Hierarchical Decomposition of the Radial Distribution Function*

This work advanced the process-structure relationship for lignin based carbon composites (LBCCs) by defining and quantifying the changes in nanoparticle shape and size, crystalline volume fraction, and density due to processing temperature and feedstock choice. This was accomplished through the development of the Hierarchical Decomposition of the Radial Distribution Function (HDRDF 3.0) software which iteratively models and optimizes structural parameters through comparison of experimental and modeled radial distribution functions (RDFs). It was found that for all studied feedstocks reduced at 1050 °C, the LBCCs possessed 4.4 – 5.6 nm spherical nanocrystallites and a 15 – 20 % crystalline volume fraction. For kraft softwood and organosolv yellow poplar lignin reduced at 1500 °C, the resultant LBCCs possessed crystalline volume fractions of 40 – 45 % with prolate ellipsoidal nanocrystallites with dimensions of 6.4 – 8.4 nm in the interplane direction and 4.4 – 6.6 nm in the intraplanar direction. Pine and switchgrass organosolv lignin reduced at 1500 °C and all feedstocks processed at 2000 °C possessed crystallites with diameters in excess of 14 nm which could

not be modelled by HDRDF 3.0 due model size limitations and the fact that the average crystallite size was vastly longer than the experimental RDF. Analysis of HR-TEM images and elemental distribution experiments suggest that the much greater amount of oxygen present in kraft softwood and switchgrass samples reduced at 1050 °C is due to a greater percentage of ether linkages and lignin monomers that persisted through pyrolysis and reduction at 1050 °C. It is also suggested that the extra ether linkages present in these samples provided some amount of longer-range order and acted as a scaffold along which the crystallites could grow into graphitic structures faster than the other samples. Process-Structure relationships defined in this work include increasing nanoparticle size and increasing crystalline volume fraction with increasing reduction temperature. The transition from spherical to ellipsoidal nanocrystallites was attributed to the adoption of graphene fragments into the nanocrystallites as reduction temperature increased.

## Impact and Significance

The impacts of this work are significant for the generation of low cost and high-performance energy storage. As the world moves away from fossil fuel sources and towards renewable and sustainable energy, we will need large-scale energy storage solutions. Since sodium is low-cost, widely globally available and has similar insertion chemistry to lithium, it is a promising candidate. Na-ion batteries will play a central role in applications where lithium is cost prohibitive and extremely high energy density is not much of a concern, such as electric smart-grid support and large-scale stationary energy storage for solar and wind farms. Since the traditional graphitic anode is the bottleneck in achieving a high-performance Na-ion battery, research into defining the process-structure-property-performance (PSPP) relationships for sustainable and domestic hard carbon anodes as well as the Na-ion storage mechanisms inside them is crucial. This work states that high performance sodium and lithium ion battery anodes can be manufactured from lignin with the correct processing conditions. There is tremendous opportunity for application of these LBCC anodes in large scale energy storage for electric grid support and storage of renewable energy.

As nanoscience progresses and nanomaterials become more complex with additional phases and extensive mesoscale structure, determining the structural and physical properties with experimental techniques alone becomes a larger challenge. There is an urgent need for rapid and iterative model refinement of nanomaterials to aid materials scientists in understanding the local structure of their nanomaterials. The development of HDRDF 3.0 extends the capabilities of previous versions by allowing arbitrary particle geometry, structural parameter refinement via conjugate gradient optimization, and

utilization on parallel computing architectures. HDRDF 3.0 was developed with generalization in mind as to be applicable to a myriad of nanoscale systems and is a timely and pertinent addition to modeling software for material scientist studying local structure of nanomaterials.

## Future Work

This work used computational materials modelling to define process-structure relationships for lignin-based carbon composites and Na-ion storage mechanisms when the LBCCs are used as anodes in Na-ions batteries. With these insights it would be useful to synthesize LBCCs with the suggested parameters and implement them as an anode in Na-ion batteries for experimental testing.

Additionally, visual analysis of HR-TEM images of kraft softwood and switchgrass LBCCs reduced at 2000 °C show onion-like crystallites, as well as rod-like structures that could be multi-walled carbon nanotubes. The literature reports excellent surface functionalization with carbon nano onion which opens up new fields of research into biosensors, bioimaging, and environmental remediation. Others in literature report large increases in capacitance using functionalized carbon nano onions as electrode materials. Mutli-walled carbon nanotubes have myriads of applications including use in nanoelectronics, batteries and capacitors, solar cells, and additives to polymers due to their excellent thermal and electric conductance. All of the previous applications are highly dependent upon the structure of the carbon nano onions/nanotubes which is controlled by the choice of lignin feedstock and reduction temperature. Further classification of these structures could prove very profitable.

HDRDF 3.0 has been established as a physics based tractable model for rapid modelling and iterative refinement of complex nanomaterials. HDRDF 3.0 was built modularly for easy updating and customization. Adding modules for polydispersity, multiphase (>3) use, as well as voids and porosity in the mesoscale would be beneficial and make HDRDF 3.0 applicable in even more situations. Finally, adding a module for layered 2D materials would be wise as many modern advances in nanomaterial science are happening in this area.

# VITA

Dayton G. Kizzire grew up in rural Ozark, Missouri near the Mark Twain National Forest with parents Lori and Billy Trimble. He enrolled at Missouri State University where he obtained his bachelor's in Physics in 2014 and Masters in Materials Science in 2016. He then traveled to Knoxville, Tennessee to accept a graduate research assistantship in the research group of Dr. David Keffer and Dr. David Harper. In this research group he focused on modelling lithium and sodium in sustainable lignin-based carbon composite anodes and the development of software for determining process-structure-property-performance relationships. His Ph.D. studies resulted in three publications and a novel software tool, HDRDF.